AFRL-AFOSR-VA-TR-2018-0390

Extremely High Quantum Efficiency and High Purity Rare-Earth-Doped Crystals for Solid-State Laser Cooling - Material Synthesis and Characterization

Mansoor Sheik-Bahae
UNIVERSITY OF NEW MEXICO

10/05/2018
Final Report

Air Force Research Laboratory
AF Office Of Scientific Research (AFOSR)/ RTB1
Arlington, Virginia 22203
Air Force Materiel Command

REPORT DOCUMENTATION PAGE

Form Approved
OMB No. 0704-0188

PLEASE DO NOT RETURN YOUR FORM TO THE ABOVE ORGANIZATION.

1. REPORT DATE *(DD-MM-YYYY)*	**2. REPORT TYPE**	**3. DATES COVERED** *(From - To)*
01/10/2018	Final Performance Report	15/7/2015 to 14/7/2018

4. TITLE AND SUBTITLE
Extremely High Quantum Efficiency and High Purity Rare-Earth-Doped Crystals for Solid-State Laser Cooling: Material Synthesis and Characterization

5a. CONTRACT NUMBER
FA9550-15-1-0241

5b. GRANT NUMBER
FA9550-15-1-0241

5c. PROGRAM ELEMENT NUMBER

6. AUTHOR(S)
Mansoor Sheik-Bahae, Professor
Dept. of Physics and Astronomy

5d. PROJECT NUMBER

5e. TASK NUMBER

5f. WORK UNIT NUMBER

7. PERFORMING ORGANIZATION NAME(S) AND ADDRESS(ES)
UNIVERSITY OF NEW MEXICO
OFFICE OF SPONSORED PROJECTS
1700 LOMAS BLVD NE
ALBUQUERQUE NM 87106-3807
(505) 277-4550

8. PERFORMING ORGANIZATION REPORT NUMBER

9. SPONSORING/MONITORING AGENCY NAME(S) AND ADDRESS(ES)
Dr. Ali Sayir
AF OFFICE OF SCIENTIFIC RESEARCH
875 NORTH RANDOLPH STREET, RM 3112
ARLINGTON VA 22203-1954

10. SPONSOR/MONITOR'S ACRONYM(S)

11. SPONSOR/MONITOR'S REPORT NUMBER(S)

12. DISTRIBUTION/AVAILABILITY STATEMENT

DISTRIBUTION A: Distribution approved for public release.

13. SUPPLEMENTARY NOTES

14. ABSTRACT

This project concerned investigating the growth and characterization of extremely high-purity low-phonon energy crystals doped with rare-earth ions (ytterbium, thulium and holmium). The overall goals are: (1) achieving lower temperatures (approaching 70K and beyond), (2) improving efficiency, and (3) enhancing the cooling power (density). The recent record cooling studies have been obtained in high-purity Yb-doped YLiF4 (YLF) crystals. Further advances in this field should address material selection and synthesis involving (a) smaller ground state manifold splitting (Stark splitting), (b) higher doping concentration without degrading the external quantum efficiency (EQE), (c) the use of dopants with smaller energy gap such as Tm, Ho and Dy, and (d) mitigation of parasitic absorption by identifying the impurity source and purifying the starting materials. In this project, we closely collaborate with Dr. Markus Hehlen at Los Alamos National Laboratory (LANL) who is the world leading material scientist in RE-doped crystals for optical refrigeration.

15. SUBJECT TERMS

16. SECURITY CLASSIFICATION OF:			**17. LIMITATION OF ABSTRACT**	**18. NUMBER OF PAGES**	**19a. NAME OF RESPONSIBLE PERSON**
a. REPORT	**b. ABSTRACT**	**c. THIS PAGE**			**19b. TELEPHONE NUMBER** *(Include area code)*

DISTRIBUTION A: Distribution approved for public release.

3nd (Final) Performance Report
September 2018

Grant FA9550-15-1-0241
Program Manager: Dr. Ali Sayir (AFOSR)

Extremely High Quantum Efficiency and High Purity Rare-Earth-Doped Crystals for Solid-State Laser Cooling: Synthesis and Characterization

PI: Mansoor Sheik-Bahae (University of New Mexico- UNM)
Co-Investigator/Collaborator: Markus Hehlen (UNM/LANL)

This project concerned investigating the growth and characterization of extremely high-purity low-phonon energy crystals doped with rare-earth ions (ytterbium, thulium and holmium). The overall goals are: (1) achieving lower temperatures (approaching 70K and beyond), (2) improving efficiency, and (3) enhancing the cooling power (density). The recent record cooling studies have been obtained in high-purity Yb-doped $YLiF_4$ (YLF) crystals. Further advances in this field should address material selection and synthesis involving (a) smaller ground state manifold splitting (Stark splitting), (b) higher doping concentration without degrading the external quantum efficiency (EQE), (c) the use of dopants with smaller energy gap such as Tm, Ho and Dy, and (d) mitigation of parasitic absorption by identifying the impurity source and purifying the starting materials. In this project, we closely collaborate with Dr. Markus Hehlen at Los Alamos National Laboratory (LANL) who is the world leading material scientist in RE-doped crystals for optical refrigeration. We also continue our close collaboration with Prof. Mauro Tonelli's group at the University of Pisa (Italy). In the second year, we sought two new international collaborations with Dr. Dorota Pawlak from Instytut Technologii Materiałów Elektronicznych (ITME) in Poland, and Sonia Baldochi from Instituto de Pesquisas Energéticas e Nucleares (IPEN) in Brazil.

Laser cooling in solids or Optical Refrigeration (based on anti-Stokes luminescence) has advanced immensely in the last decade. First observed in 1995 as a scientific curiosity at Los Alamos National Lab, the field has been propelled forward by recent demonstration of cooling to below 100K from room temperature by the PI's group at UNM, thus introducing the world's first all-solid-state cryocooler without moving parts and vibrations. Implications for such a transformative technology are vast in applications ranging from cooling air-borne and space-borne sensors to superconducting electronics by such compact and light-weight cryo-refrigerators. Two major areas of research include laser cooling in (I) rare earth (RE-) doped materials, and (II) semiconductors. Our proposed tasks in this project is concerned exclusively with the former.

Overview of Year 3 Results:

I. We reported the demonstration of the first all-solid-state cryocooler using optical refrigeration in Yb:YLF as published in Light: Science and Applications (Nature). This publication received tremendous attention in the scientific media, such as Nature Photonics (News & Views), and Laser Focus World (cover page story). See photo.
II. By conducting delicate experiments, we observed a strong temperature dependence in the background parasitic absorption in Yb:YLF. This discovery explains the low temperatures that we have reached during optical refrigeration in these crystals.
III. We have fully characterized various mid-IR materials such as Tm:YLF, Tm:BYF, Ho:YLF for optical refrigeration and radiation-balanced lasers. The temperature dependent spectroscopic studies were used to arrive at the minimum achievable temperature (MAT) for each crystal.
IV. Our high-purity crystal growth effort using Bridgeman technique is now operational. With engineering various crucibles, we have gained an thorough understanding of the conditions for growth of single-crystal YLF and LLF materials.

Below, we present details of the Year-3 efforts in the context of our overall goal of this project.

Progress in cooling Yb:YLF crystals:

a. A solid-state cryocooler- at last!

Let's recall that the cooling efficiency η_c is given by the ratio of the cooling power (P_{cool}) and absorbed power (P_{abs}):[8]

$$\eta_c = \frac{P_{cool}}{P_{abs}} = \eta_{ext}\eta_{abs}\frac{\lambda}{\bar{\lambda}_f} - 1, \quad (1)$$

where $\eta_{ext} = \eta_e W_r/(\eta_e W_r + W_{nr})$ is the external quantum efficiency and $\eta_{abs} = \alpha_r(\lambda)/[\alpha_r(\lambda) + \alpha_b(\lambda)]$ is the absorption efficiency. Here, W_r and W_{nr} are the radiative and non-radiative decay rates of the emitting state, respectively; η_e is the fluorescence escape efficiency; $\alpha_r(\lambda)$ is the resonant absorption coefficient of the cooling transition; and $\alpha_b(\lambda)$ is the parasitic background absorption coefficient. The radiative process of cooling by anti-Stokes fluorescence competes with a variety of non-radiative processes that reduce η_{ext} and η_{abs} by multiphonon relaxation of the emitting state (W_{nr}) and absorption

by impurities (α_b), respectively. Yb^{3+}-doped solids have received particular attention because Yb^{3+} can be excited with high-power lasers of approximately 1 μm wavelength and can emit with high quantum efficiency due to its simple energy-level structure. However, laser cooling of Yb^{3+}-doped solids to cryogenic temperatures is only practical if $\eta_{ext}\eta_{abs}$ exceeds 0.98–0.99, a challenging requirement that necessitates a cooling crystal with exquisite purity[9]. High-purity $YLiF_4$ crystals doped with 10 mol% Yb^{3+} (YLF:10%Yb) have recently been cooled to 91 K by exciting them with a laser tuned to the E4→E5 crystal-field transition of Yb^{3+} at 1020 nm [10].

Most solid-state laser cooling studies to date have focused on the optical refrigeration of the laser-cooling material itself[4] or a load that is transparent to fluorescence[11]. For practical applications, however, it is necessary for the laser-cooling material to refrigerate an attached arbitrary external payload, such as a sensor or electronic component. The primary challenges for advancing from a basic laser-cooling setup to a practical optical cryocooler device involve: (1) managing the numerous heat and radiation flows in the system and (2) providing a sturdy, thermally insulating support structure for the laser-cooled assembly. In this article, we address these challenges and describe the design and first experimental demonstration of a solid-state optical cryocooler capable of refrigerating a HgCdTe infrared sensor to 135 K. This device is the only solid-state cooling device that works in the cryogenic regime, *i.e.*, in the temperature range of liquid cryogens, such as Xe, with a boiling point of 166 K. The most common solid-state refrigerators, thermoelectric coolers, cannot achieve temperatures nearly as low as 135 K.

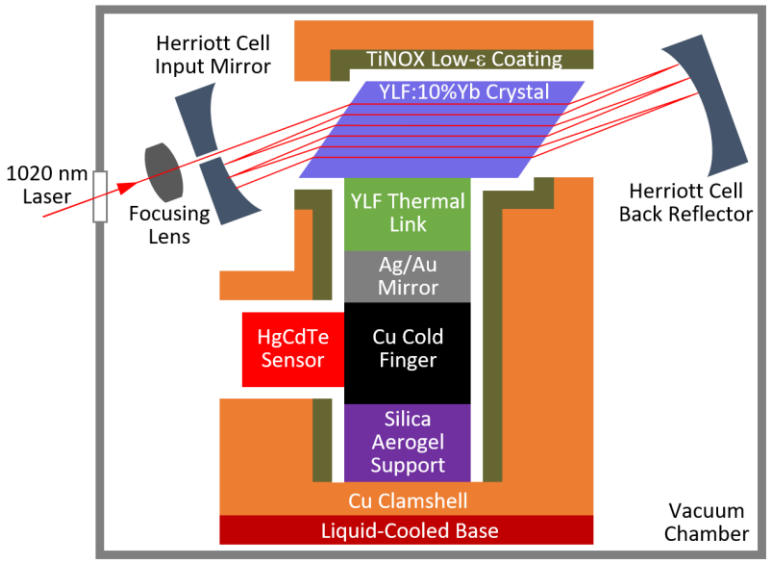

Figure 1: Block diagram (not to scale) showing the components of a solid-state optical cryocooler. The laser-cooling material (blue) is placed inside an astigmatic Herriott cell to provide for multi-pass excitation by the pump laser. The sensor payload (red) is connected via a coldfinger (black), a mirror (grey), and thermal link (green) to the laser-cooling material. A support element (purple) provides the mounting of this assembly within

a closely-fitting clamshell (orange), which is lined with a low-emissivity coating (olive) and mounted to a liquid-cooled base (dark red). The cryocooler is contained within a vacuum chamber (grey).

Figure 1 shows a block diagram of the solid-state optical cryocooler architecture used in this study. The payload is attached via a coldfinger, mirror, and thermal link to the laser-cooling material. This assembly (refrigerator cold side) is mounted with a support element and surrounded by a closely fitting clamshell (refrigerator hot side), which is lined with a low-emissivity coating. The breakthrough performance of the present solid-state optical cryocooler is enabled by the materials and geometries of both the thermal link and support element combined with a high-performance YLF:10%Yb^{3+} crystal. The design of various components and the performance of the optical cryocooler are discussed in detail in the following sections.

Optical components

A YLF:10%Yb laser-cooling crystal was cooled to 91 K in a previous study[10]. The cooling crystal was cut so that the linearly polarized pump laser has $\vec{E} \parallel \vec{c}$ because the absorption cross section of the E4→E5 crystal-field transition in a YLF:Yb crystal at 1020 nm is ~1.7× greater in this geometry than that with $\vec{E} \perp \vec{c}$ polarization[12].

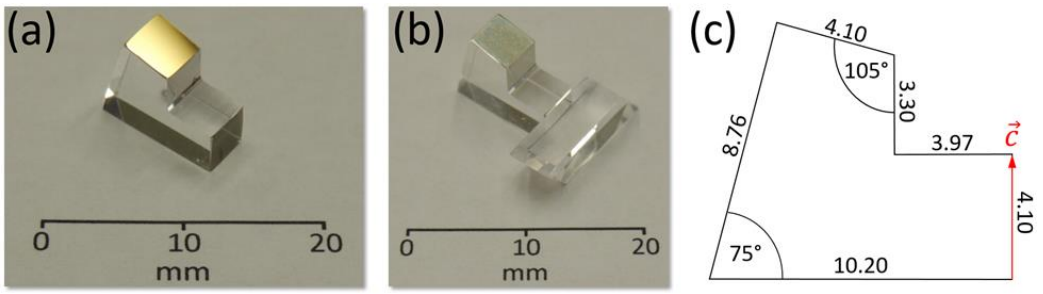

Figure 2: *Geometry, fabrication, and bonding of YLF thermal link. (a) Fabricated YLF thermal link with sputtered Ag/Au mirror on the cold-finger interface. (b) YLF thermal link AFB-bonded to the Brewster-cut YLF:10%Yb cooling crystal. (c) Cross sectional view and dimensions (in mm) of the $\delta = 15^o$ geometry with a 90° inside angle. The dimension in the orthogonal direction is 4.10 mm. The orientation of the $\vec{c}$ axis is indicated, and it is parallel to the $\vec{c}$ axis of the YLF:10%Yb crystal.*

The thermal link was fabricated from a Czochralski-grown undoped YLF crystal boule (AC Materials, Tarpon Springs, FL), which was found to have low parasitic background absorption coefficients of $\alpha_b(\vec{E} \parallel \vec{c}) = 9.6 \times 10^{-5}$ cm^{-1} and $\alpha_b(\vec{E} \perp \vec{c}) = 4.4 \times 10^{-5}$ cm^{-1}, as determined by exposing the sample to a 1020-nm laser (43 W) and measuring the resulting temperature increase relative to a reference heat load using a

thermal camera (Nanocore 640, L3 Communications Corporation, Garland, TX, USA). The YLF thermal link was fabricated such that its $\vec{c}$ axis was aligned parallel to the $\vec{c}$ axis of the YLF:10%Yb crystal at the respective mating interface (Figure 1). This crystallographic alignment minimized the thermal stresses induced by the anisotropic coefficients of thermal expansion (CTE) of YLF. The thermal link surface that was attached to the coldfinger was subsequently coated with a metallic mirror by first etching the YLF in an argon plasma followed by sputter deposition of 200 nm of silver, followed by 200 nm of gold. This produced a silver mirror with high reflectance on the inside of the thermal link that was protected from oxidation by the gold layer. Figures 2a and 2b show the mirrored YLF thermal link before and after Adhesive-Free Bonding[13,14] (AFB® by Onyx Optics, Inc., Dublin, CA) to the YLF:10%Yb crystal, respectively. The elevated temperatures during the AFB process caused interdiffusion of the Ag and Au layers, as shown by the discoloration of the external gold layer in Figure 2b. No discoloration of the optically important inside Ag mirror was observed. Furthermore, no mechanical failure was observed when temperature cycling an equivalent assembly 22 times from 300 K to 75 K (at -6.9 K/min) and back to 300 K (at +21.6 K/min), demonstrating that a thermo-mechanically reliable AFB between undoped YLF and YLF:10%Yb was achieved.

Silica aerogels were synthesized by a sol-gel process, followed by drying in supercritical methanol, which yielded hydrophobic aerogels that reversibly adsorbed <2 wt% water during long-term storage in ambient air[15]. This process also allowed custom aerogel shapes to be directly molded during synthesis. We fabricated hydrophobic silica aerogels with a 0.1 g/cm^3 density in the shape of 5 mm diameter × 5 mm tall cylinders as the basic support element. The samples were found to absorb $< 2 \times 10^{-4}$ of the incident power of a 1015-nm laser and were therefore expected to produce a negligible heat load when exposed to YLF:Yb fluorescence.

The solid-state optical cryocooler was placed in a vacuum chamber (5×10^{-7} Torr), and the YLF:10%Yb crystal was excited by a linearly-polarized continuous-wave fiber laser (IPG Photonics, Inc., custom-made) that provided 47 W at 1020 nm. The temperature of the coldfinger was monitored with a calibrated silicon diode (LakeShore Cryotronics, DT-670-SD) located in the coldfinger base. In addition, non-contact differential luminescence thermometry (DLT)[3] was used to monitor the temperature of the cooling crystal by collecting fluorescence with a multimode optical fiber inserted flush with the clamshell wall near the YLF:10%Yb crystal.

Thermal model

The dynamics of the observed temperature changes of the cooling crystal and coldfinger follow an intricate interplay between the absorbed laser power, cooling efficiency, parasitic losses (due to fluorescence absorption) at interfaces, radiative loads, conductive loads and useful loads (*e.g.,* heat lift from the sensor). A rigorous model that numerically solves the 3-dimensional heat equation including the exact structure of the

optical cooler could, in principle, reproduce the observed thermal dynamics. However, we were able to determine the essential features and underlying parameters by considering a simple 3-element model, as depicted in Figure 3, that consisted of the YLF:Yb cooling crystal (at temperature T_x) connected to the coldfinger (at temperature T_f) by a thermal link (at temperature T_l), which in this case, was also constructed from a YLF (undoped) crystal.

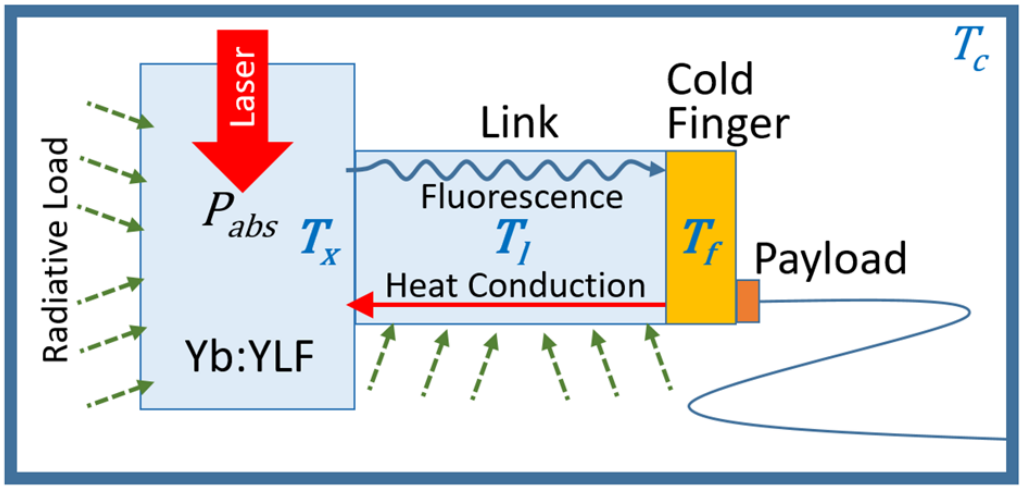

Figure 3: *Three-body thermal model of the optical cryocooler. The model consists of a cooling crystal (YLF:Yb) at temperature T_x and a thermal link (YLF) with a mid-length temperature of T_l connected to a copper coldfinger at temperature T_f. These elements are placed in a vacuum clamshell whose walls are coated with low-emissivity materials at a constant (ground) temperature of T_c.*

Assuming that the adhesive-free bond between the cooling crystal and thermal link introduces negligible thermal resistance and parasitic loss, the equations governing the temperature evolution of the three elements are approximated as follows:

$$C_x \frac{dT_x}{dt} = -\eta_c(T_x)\, P_{abs}(T_x) + \epsilon_x \sigma (T_c^4 - T_x^4) A_x + K_l(T_x)(T_l - T_x) \tag{2}$$

$$C_l \frac{dT_l}{dt} = -K_l(T_x)(T_l - T_x) + \epsilon_l \sigma (T_c^4 - T_l^4) A_l + K_f(T_l)\left(T_f - T_l\right) \tag{3}$$

$$C_f \frac{dT_f}{dt} = -K_f(T_l)\left(T_f - T_l\right) + \epsilon_f \sigma \left(T_c^4 - T_f^4\right) A_f + \beta_l \eta_{ext}(T_x) P_{abs}(T_x) + P_{lift}\,, \tag{4}$$

where $C_{x,l,f} = V_{x,l,f} C^v_{x,l,f}(T)$, with $V_{x,l,f}$ and $C^v_{x,l,f}$ denoting the known volume and heat capacity (J/K/m^3), respectively, of the cooling crystal (x), link (l), and coldfinger (f). The temperature dependence of the YLF heat capacity is taken from Ref. [16]. $P_{abs}(T) =$

$P_{in}\eta_{cpl}$ is the absorbed power drawn from the incident power P_{in} (at λ=1020 nm). Here, $\eta_{cpl} = 1 - \exp(-2N_{rt}\alpha_r(\lambda, T)L_x)$ is the laser coupling efficiency, where N_{rt} is the number of roundtrips the laser makes through the crystal of length L_x placed inside the astigmatic Herriot cell[16] and $\alpha_r(\lambda, T_x)$ is the resonant absorption coefficient of the Yb^{3+} crystal-field transition[16]. $K_l(T_l) = 2\kappa A/L_l$ is the effective thermal conductance of the link with a cross-sectional area of A and an effective length L_l. The factor of 2 arises from the fact that T_l is the temperature of the link halfway between the crystal and the coldfinger. $\kappa(T_l)$ is the temperature-dependent thermal conductivity of the thermal link (undoped YLF).[17] A_x, A_l, and A_f denote the total surface area of the cooling crystal, link, and cold-finger, respectively. $\epsilon_x \approx \epsilon_l$ are the *effective* emissivities, $\varepsilon/(1+\chi)$, of YLF in a tight clamshell coated with a low emissivity (ε_c) TiNOX solar absorber (Almeco GmbH, Bernburg, Germany) held at constant temperature T_c and ϵ_f is the effective emissivity of the copper coldfinger. Here, $\chi = (1-\varepsilon_c)\varepsilon_l A_l/\varepsilon_c A_c$ (Ref. 11), where ε_l and ε_c are the emissivities and σ is the Stefan-Boltzmann constant. β_l represents the fraction of the total fluorescence power that effectively leaks though the link and is consequently absorbed by the coldfinger. P_{lift} is the useful thermal load (payload heat lift) and small parasitic load from the sensor wires and aerogel supports.

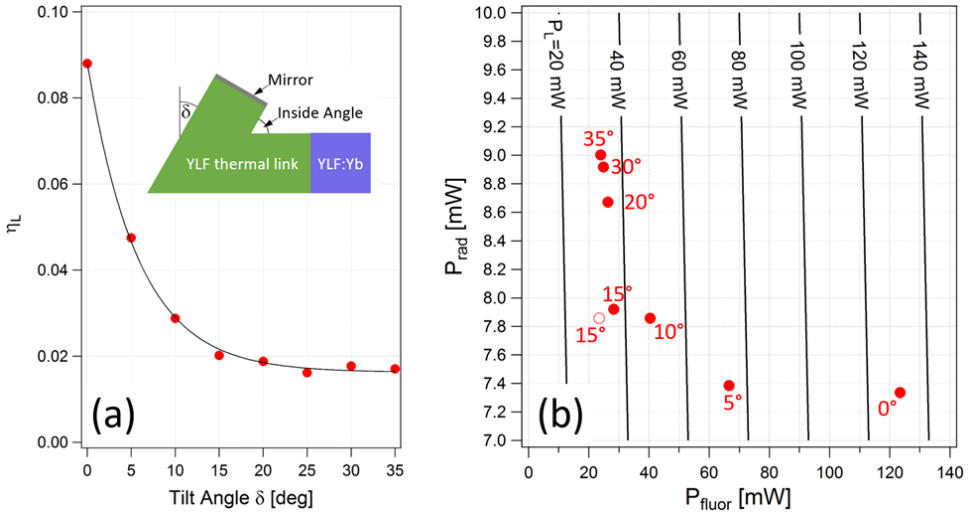

Fig. 3 Optimization of the YLF thermal link geometry. (a) The fraction of fluorescence power reaching the link/mirror interface η_L for different tilt angles δ as obtained from a raytracing simulation (red circles) and a fit of the data to a single exponential function (black line). The inset shows a cross-sectional view of the kinked thermal link (green) attached to the YLF:Yb laser-cooling crystal (blue) and coated with a mirror on the interface that attaches to the coldfinger (see Figure 1). The tilt angle δ is indicated. (b) Calculated heat load on the thermal link from thermal radiation P_{rad} versus the optical heat load due to fluorescence absorption at the link mirror P_{fluor} for links with different δ values. The calculation assumed link and clamshell temperatures of 135 and 300 K, respectively, P_{in}=47 W, η_{cpl} =0.999, η_{ext} =0.996, and R_m =0.97. Link geometries with an inside angle of $(90^o - \delta)$ and 90^o are shown as filled and open circles. Lines of constant total heat load $P_L = P_{fluor} + P_{rad}$ are indicated.

Cooling crystal and Herriott cell

As shown in Eq. (1), the cooling power of a solid-state optical refrigerator linearly scales with the laser power absorbed by the cooling crystal (YLF:Yb), $P_{abs} = P_{in}\eta_{cpl}$, which in turn depends on N_{rt}, α_r, and L_x. The temperature dependence of α_r scales as $\alpha_r(T_x) \propto \left[1 + \exp\left(\delta E_g / k_B T_x\right)\right]^{-1}$, where $\delta E_g \approx 460$ cm^{-1} is the width of the $^2F_{7/2}$ ground-state multiplet in YLF:Yb and k_B is the Boltzmann constant[16]. The decrease of α_r at low temperatures requires N_{rt} to be ~13× greater at 135 K than at 300 K to realize the same P_{abs}. To realize a large P_{abs}, the Brewster-cut YLF:10%Yb crystal was placed inside an astigmatic Herriott cell[16] formed by a concave spherical input mirror ($R = 50$ cm) and a cylindrical back reflector ($R_x = \infty$, $R_y = 50$ cm) with the laser focused into the cell with a spherical lens ($f = 5$ cm) through a 400 μm diameter center hole in the input mirror. We estimate $N_{rt} \approx 40$ in the final configuration, which yields $\eta_{cpl} > 0.9999$ with $L_x = 1.11$ cm and $\alpha_r = 0.12$ cm^{-1} at 1020 nm and 135 K for $\vec{E} \parallel \vec{c}$.

Thermal link

Attaching the payload directly to the YLF:Yb crystal is impractical. Although this would provide an excellent thermal contact, the payload would be directly exposed to YLF:Yb fluorescence and absorb radiation that could exceed P_{cool}. Therefore, a transparent thermal link was inserted between the YLF:Yb crystal and payload (Figure 1) to reduce the amount of fluorescence reaching the payload while maintaining an efficient thermal path between the payload and YLF:Yb crystal[18,19]. The thermal, mechanical, and optical properties of the resulting interface between the YLF:Yb crystal and thermal link require careful consideration. The use of adhesives to bond the two elements can introduce optical absorption and corresponding heating. We avoided this by bonding the cooling crystal and thermal link by van-der-Waals forces in an Adhesive-Free Bond (AFB®)[13,14]. Although sapphire is an attractive thermal-link material due to its low optical absorption and high thermal conductivity ($\kappa \approx 400$ W/m·K at 100 K [20]), our preliminary experiments exploring the AFB of YLF:10%Yb and sapphire found frequent bond failures upon thermal cycling from 300 to 77 K. The stress at the AFB interface induced by a temperature change ΔT is proportional to $\Delta T \Delta\alpha$, where $\Delta\alpha$ is the difference in the coefficients of thermal expansion (CTE) of the two bonded materials[21]. The CTE of sapphire ($\alpha_a = 5.22 \times 10^{-6}$ K^{-1} and $\alpha_b = 5.92 \times 10^{-6}$ K^{-1} at 296 K [20]) and YLF ($\alpha_a = 13.0 \ldots 14.3 \times 10^{-6}$ K^{-1} and $\alpha_c = 8.0 \ldots 10.1 \times 10^{-6}$ at 300 K [17,22]) indicate a $\Delta\alpha \approx (8 - 9) \times 10^{-6}$ K^{-1} and a resulting stress of 180–200 MPa for $\Delta T = 223$ K, which exceeds the tolerable stress of mechanically reliable AFB composites of dissimilar materials[21] by ~10×. We therefore chose to use undoped YLF instead of sapphire as the thermal link material, nominally yielding $\Delta\alpha \approx 0$ and thus a stress-free adhesive-free bond between the YLF:10%Yb cooling crystal and the undoped YLF thermal link. However, this results in a ~14× lower thermal conductivity of

YLF ($\kappa_a = 24$ W/m·K and $\kappa_c = 34$ W/m·K at 100 K [17]) than that of sapphire. The undoped YLF thermal link, therefore, must be as short as possible to minimize the temperature difference between the payload and YLF:Yb crystal, while still providing good fluorescence light rejection.

Given these constraints, we optimized the YLF thermal link in the geometry of a short kinked YLF waveguide (Figure 4a, inset). The goal was to minimize the total heat load introduced by the thermal link $P_L = P_{fluor} + P_{rad}$, where P_{fluor} is the fraction of fluorescence power absorbed at the thermal link mirror surface (see Figure 1) and P_{rad} is the heat load due to radiative heat transport from the coated clamshell surface (warm) to the thermal link (cold). Our measurements have shown that negligible heat is produced by the absorption of the fluorescence in the bulk of the YLF thermal link. We performed an optical raytracing simulation of the light transport in the thermal link using the FRED Optical Engineering software (Photon Engineering, LLC, Tucson, AZ, USA). A 4.1 × 4.1 mm^2 link cross section was chosen to match the width of the existing YLF:10%Yb crystal. The model used $\bar{\lambda}_f = 1004.7$ nm as measured for YLF:Yb at 135 K, and a corresponding averaged refractive index of $n = (2n_o + n_e)/3 = 1.456$, where $n_o = 1.448$ and $n_e = 1.471$ [23], was used for both undoped YLF and YLF:10%Yb. The fluorescence was represented by 10^6 rays that were uniformly and isotropically emitted within the attached YLF:Yb crystal. As shown in Figure 4a, an exponential decrease of the fraction of fluorescence power reaching the link/mirror interface η_L occurs when increasing the tilt angle δ; η_L does not significantly change for $\delta > 15^o$. This simulation yields $P_{fluor} = P_{in}\eta_{cpl}\eta_{ext}\eta_L(1 - R_m)$, where R_m is the reflectance of the mirror, which is set as 0.97 for the sputtered silver layer used in this study, and $P_{in} = 47$ W, η_{cpl} =0.999, and η_{ext} =0.996 are assumed. The radiative heat load on the thermal link is approximately $P_{rad} = \varepsilon_l A_l \sigma(T_c^4 - T_l^4)/(1 + \chi)$. A 1-mm gap is assumed between the thermal link and the TiNOX-coated clamshell surfaces as well as $\varepsilon_l = 0.9$ (from CaF_2 [24]), $\varepsilon_c = 0.05$ (TiNOX solar absorber datasheet), $T_l = 135$ K, and $T_c = 300$ K. Figure 4b plots P_{rad} *vs.* P_{fluor} for thermal links with different δ. The $\delta = 15^o$ design achieves the lowest P_L, whereas links with a smaller δ have a significantly larger P_{fluor} due to the greater η_L, and links with greater δ have a slightly larger P_{rad} due to their larger surface areas A_l and A_c. The link performance is slightly improved by providing a 90° inside angle (see inset Figure 4a), a geometry that is also more favorable for fabrication than geometries with smaller inside angles. The final thermal link design (Figure 2c) is estimated to produce a total heat load of $P_L = 31.3$ mW, of which 75% is due to residual mirror absorption. Compared with a typical $P_{cool} = 470$ mW (for $P_{in} = 47$ W, $\eta_{cpl} \approx 1$, and η_c=0.01), the heat load introduced by the YLF thermal link is relatively small.

Silica aerogel supports

The laser-cooled assembly consisting of the YLF:Yb crystal, YLF thermal link, mirror, coldfinger, and payload (Figure 1) must be mounted within the closely fitting clamshell structure in a manner that introduces minimal thermal conduction from the clamshell to the cooled assembly, is mechanically reliable, and can be easily assembled. Earlier experiments using silica optical fibers with sharpened tips as support elements were difficult to assemble and mechanically unreliable. The new approach implemented in this study uses several silica aerogel cylinders to support the cooled assembly under the coldfinger. Silica aerogels are open-celled mesoporous SiO_2 networks with low mass densities of typically 0.01–0.2 g/cm^3 as well as low optical absorption in the visible and near-infrared spectral range. Pure SiO_2 aerogels have low thermal conductivities of ~0.004 W/m·K (at 300 K) and ~0.001 W/m·K (at 100 K) in a vacuum[25], making them attractive for use as support structures in optical cryocoolers. The laser-cooled assembly (19.1 g total weight) rested on three 5 mm diameter × 5 mm tall aerogel cylinders (58.9 mm^2 total area), thus producing a pressure of 3.18 kPa. Four additional aerogel cylinders were used around the outside perimeter of the coldfinger base to laterally secure the assembly. No mechanical degradation of the aerogel cylinders was observed under these conditions, which is consistent with the compressive strength of silica aerogels, for which values of 1 MPa (0.25 g/cm^3) [26] and 0.047–0.11 MPa (0.1 g/cm^3) [27] have been reported.

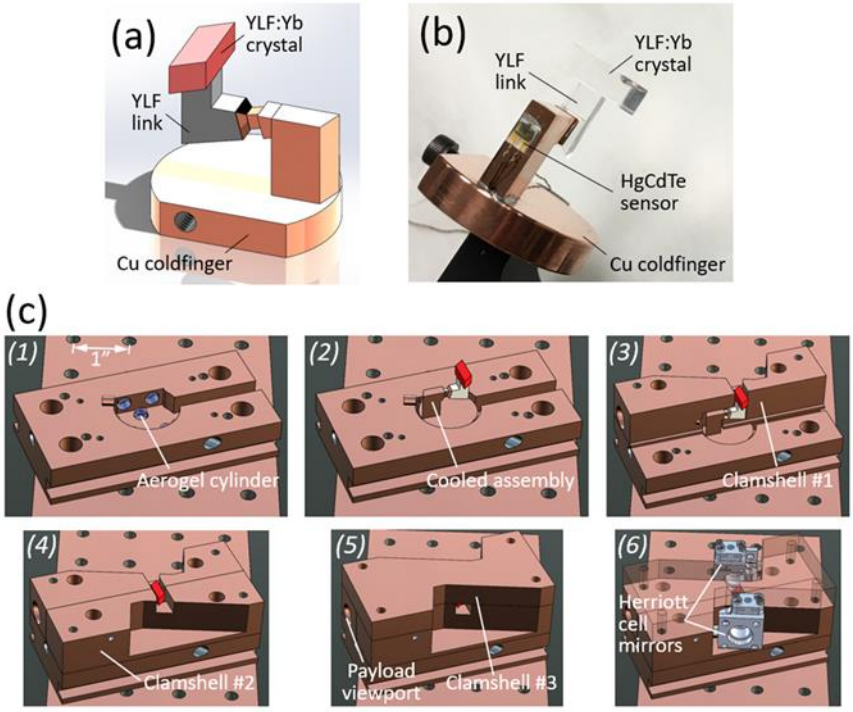

Figure 5: *Solid-state optical cryocooler design and assembly. (a) Cooled assembly consisting of a YLF:Yb crystal, YLF thermal link, and copper coldfinger. (b) Image of the cooled assembly showing the HgCdTe sensor payload attached to the coldfinger. (c) Cryocooler assembly sequence consisting of the insertion of 7 aerogel cylinders (1), placement of the cooled assembly (2),*

installation of side and top clamshell layers (3,4,5), and positioning and alignment of Herriott cell mirrors (6).

Laser-cooled assembly and clamshell

Earlier solid-state optical cryocooler designs envisioned attaching the payload directly to the coated side of the thermal link[19,28], an approach that creates significant size constraints for the placement of the support elements and potentially larger payloads. We therefore introduced a copper coldfinger in the present cryocooler, allowing for more space to accommodate larger payloads, aerogel supports, as well as other instrumentation, such as a temperature sensor and heating element. Figures 5a and 5b show the cooled assembly consisting of the YLF:Yb crystal / YLF thermal link unit and the HgCdTe infrared photo-sensor chip (InfraRed Associates, Inc.) attached to the copper coldfinger. The necked shape of the coldfinger near the thermal link interface was created to provide an optical baffle that prevented residual fluorescence from reaching the payload.

The clamshell serves as the heat sink for the fluorescence emitted by the YLF:Yb crystal and must be designed to minimize the radiative heat loads [Eqs. (2)–(4)] it imparts on the cooled assembly, which requires a geometry that closely envelops the cooled assembly to minimize the surface area and maximize χ. Figure 5c shows the assembly sequence of the layered structure, which allows for a stepwise installation of the clamshell at a separation of 1 mm around the cooled assembly. We used a TiNOX Energy solar absorber (Almeco GmbH, Bernburg, Germany) glued to the inside surfaces of the clamshell with silver epoxy to provide high absorbance of the YLF:Yb fluorescence and low thermal emissivity. The clamshell also included a viewport that provided optical access to the HgCdTe sensor payload.

Laser cooling of a HgCdTe sensor

Figure 6a shows the coldfinger temperature (measured with a silicon diode) and the cooling crystal temperature (measured by DLT) as a function of time after turning on the 1020-nm laser. The 1020 nm laser power was increased in steps from 0, 12, 25, to 47 W as a precautionary measure to reduce the potentially large temperature gradient and associated thermally induced stresses between the YLF:Yb crystal and coldfinger that develop at early times. This is evident in the stepwise decrease of the YLF:Yb crystal temperature as measured by DLT. The coldfinger temperature reached 134.9 K after 4 hours, representing the first ever demonstration of cooling a payload to the cryogenic regime using solid-state optical refrigeration. Furthermore, these data experimentally validate the various geometry and material choices for the thermal link, coldfinger, aerogel supports, and clamshell discussed above.

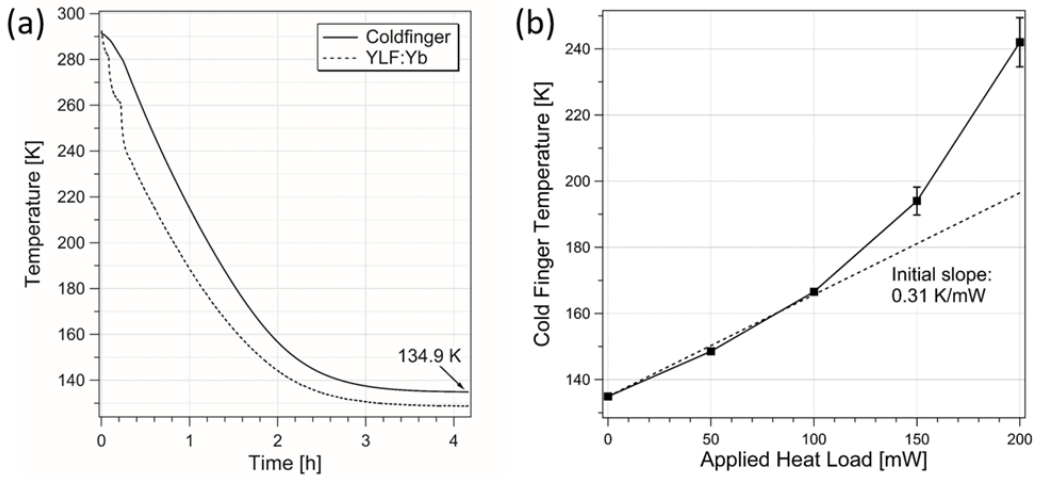

Figure 6: *Performance of the solid-state optical cryocooler. (a) Temperature of the coldfinger (solid trace) and YLF:10%Yb crystal (dotted trace) as a function of time after turning on the 1020-nm laser in steps from 0, 12, 25, to 47 W. A steady-state coldfinger temperature of 134.9 K was reached after 4 hours. (b) Heat load curve of the cryocooler pumped at 47 W, showing an initial slope of 0.31 K/mW.*

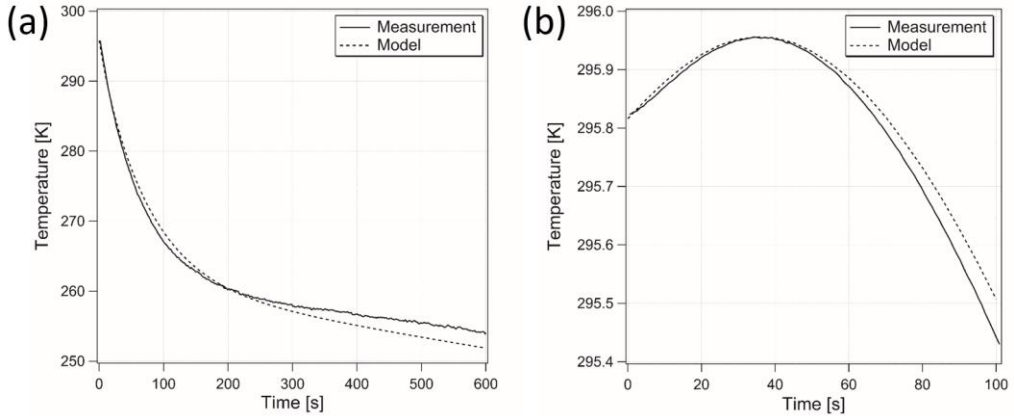

Figure 7: *(a) YLF:Yb cooling crystal temperature (T_1) and (b) copper coldfinger temperature (T_3) at early times. The measured (solid lines) and calculated (dotted lines) temperatures are shown as a function of time after turning on the 1020-nm pump laser at $t = 0$ with $N_{rt} = 1$.*

The results shown in Figure 6a were obtained without an electrical current flowing through the HgCdTe sensor, *i.e.*, without an external heat load introduced by the payload. A separate resistor installed in the coldfinger base allowed for the application of well-defined heat loads and measurement of the corresponding increase in the coldfinger temperature. Figure 6b presents the heat load curve obtained with the YLF:10%Yb crystal pumped at 47 W. The initial slope is 0.31 K/mW, a value that is characteristic for this particular cryocooler. Powering up the HgCdTe sensor through a Fourier-Transform Infrared (FTIR) spectrometer (Midac M4401) at the 134.9 K base temperature resulted in a temperature

increase of ~2.5 K, which corresponds to an estimated 8 mW heat load introduced by the active HgCdTe sensor. This value is in good agreement with the 8.8 mW heat load calculated from the 22.5 mA bias current and 17.3 Ω resistance (at 134.9 K) of the HgCdTe sensor.

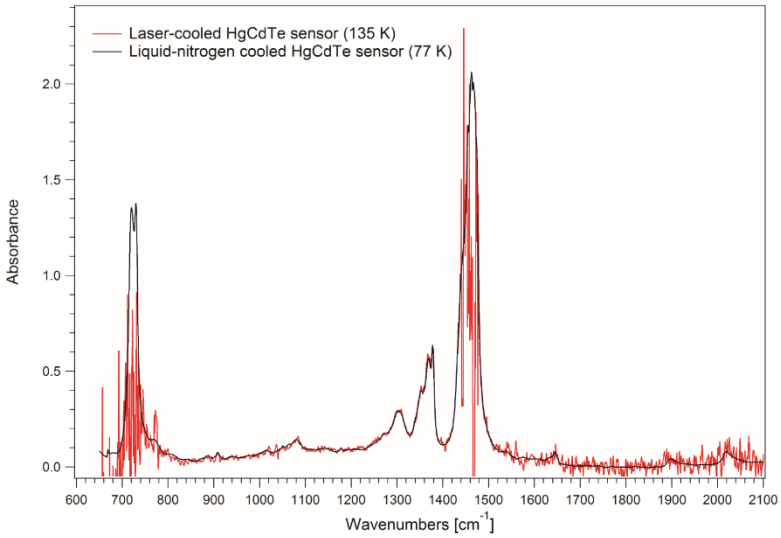

Figure 8: *FTIR spectroscopy using a laser-cooled HgCdTe infrared sensor. FTIR spectrum of a sheet of low-density poly-ethylene (LDPE) measured with the laser-cooled HgCdTe sensor (135 K, red trace) and, for comparison, an equivalent liquid-nitrogen cooled HgCdTe sensor (77 K, black trace). The larger relative noise observed at the extremes of the spectra is simply a result of the smaller signal (HgCdTe sensitivity and/or source brightness) in these regions; the noise amplitude is wavelength-independent.*

The thermal model presented above [Eqs. (2)–(4)] allows us to gain insight into the roles of the various terms in the observed temperature dynamics. The cooling crystal temperature (T_x) initially drops rapidly with the slope given by $\approx -\eta_c(T_c)\, P_{abs}(T_c)/C_x(T_x)$ before the radiative load (from the chamber) and conductive load (through the link) slow down this process, as shown in Figure 7a. The coldfinger, however, initially experiences a small temperature increase due to the small fluorescence leakage β_l at a rate given by $\approx \beta_l \eta_{ext}\, P_{abs}(T_c)/C_f(T_c)$ before cooling from the crystal reverses this process in a time scale approximated by $\tau \approx K_l(T_c)/C_l(T_c)$, as shown in Figure 7b. Beyond this point, both the crystal and cold-finger continue to cool and reach the steady-state condition with a temperature difference $(T_f - T_x)_{final} \approx 2P_{load}^{link}/K_l(T_l)$, where P_{load}^{link} denotes the total heat load power (parasitic and useful) carried through the link. The data used in Figure 7 and the corresponding fits were obtained for $N_{rt} = 1$ (one laser roundtrip). The parameters obtained from these fits are $\beta_l \approx 0.2\%$, $\eta_c(T_c) \approx 1.2\%$ at λ=1020 nm (corresponding to $\eta_{ext} \approx 0.992$), $\alpha_b \approx 2.1 \times 10^{-4}\ cm^{-1}$, and $\epsilon_x \approx \epsilon_l \approx 0.38$. The values for η_{ext} and α_b are in close agreement with previously measured values for this 10% Yb^{3+}-doped YLF crystal. β_l also agrees with the calculated value from the raytracing model. T_c was fixed at

283.15 K, which is the final measured temperature of the clamshell. With the above parameters fixed, the model predicts a final coldfinger temperature $T_f = 135.0$ K with a temperature drop of $\Delta T = T_f - T_x = 6.8$ K across the link when the number of roundtrips is increased to $N_{rt} \geq 30$, as expected in the Herriott cell arrangement. Considering the simplicity of our model, these calculated values are in excellent agreement with our observed values of $T_f = 134.9$ K and $\Delta T = 6.1$ K (Figure 6a). The above calculations assumed a negligible heat lift ($P_{lift} = 0$ mW) in comparison to the existing radiative and fluorescence loads. Furthermore, the measured initial slope of 0.31 K/mW (Figure 6b) is in good agreement with $\partial T_f / \partial P_{lift} \approx 0.31$ K/mW obtained from the model calculations.

FTIR spectroscopy with the laser-cooled HgCdTe sensor

In a final experiment, the laser-cooled HgCdTe sensor was used as part of an FTIR spectrometer and the infrared absorption spectrum of a sheet of low-density poly-ethylene (LDPE) was measured (Figure 8). This is the first demonstration of a sensor cooled by solid-state optical refrigeration used as part of a practical device. Figure 8 shows the absorbance spectrum of the same sample measured with an equivalent HgCdTe sensor cooled with liquid nitrogen to 77 K. The bandgap energy $E_g = hc/\lambda$ of this HgCdTe sensor corresponds to a cutoff wavelength of $\lambda = 16.7$ μm. The primary noise source is due to statistical fluctuations of the thermally activated dark current within the detector element. The dark current I_d is proportional to the number of carriers that are thermally excited across the bandgap and thus varies approximately as $I_d \propto \exp(-E_g/k_B T_f)$,with the corresponding noise amplitude varying as $\sqrt{I_d}$. The detector noise amplitude is therefore expected to be ~11× greater at 135 K than at 77 K, which is consistent with the observed lower signal-to-noise ratio in the measurement using the laser-cooled sensor.

b. Understanding the data on Yb:YLF co-doped with Tm

As reported in our 2nd progress report, upon performing power cooling experiments on a 5% Yb: YLF sample, with dilute Tm co-doping (0.0016%), record optical cooling down to 87 K was observed, a temperature much lower than the MAT of ~ 98 K predicted from the model, based on room-temperature measurements of external quantum efficiency and background absorption, for this sample. Endothermic energy-transfer processes and high-resolution investigations of resonant absorption at low temperatures were not able to explain the remarkable efficiency enhancement observed in power cooling experiments.
However, so far, in the cooling efficiency model we have assumed background absorption as temperature independent: these observations may be indicative that such an approximation is not valid and/or not universal. A decrease of background absorption with temperature, indeed, would result in slower decrease of absorption efficiency as the temperature lowers, pushing down the MAT.
In Year 3, in order to understand the unexpected Yb-Tm result, we focused on investigating the temperature dependence of background absorption, setting up a low-temperature

LITMoS. In this method, the sample will be cooled below RT (room temperature), using a cryostat, and pump-induced temperature changes will be measured as a function of pumping wavelength at different sample temperatures. From direct measurements of cooling efficiency, temperature dependence of background absorption and EQE can then be extracted.

Implementation of such an experiment, however, presents several experimental challenges, due to the small magnitude of the quantities to be measured and the fine tuning of thermal resistance which is required.

In order to better understand the role each of the parameters is playing, the pump-induced temperature change to be measured can be written as: $\Delta T = \frac{P_{abs}(\lambda,T)\cdot\eta_c(\lambda,T)}{k}$ where $P_{abs}(\lambda,T)$ is the absorbed pump power at the given excitation wavelength λ and sample temperature T, η_c is the cooling efficiency and k a parameter which accounts for the heat load onto the sample. In order to maximize ΔT, external heat loads onto the sample need to be minimized. At the same time, however, a sufficient thermal contact with the cryostat is required to vary the sample temperature. This is a crucial point of this method, which requires delicate fine trade-off tuning of thermal resistances in order to work out.

As a result of Boltzmann distribution and phonon broadening, in the long wavelength tail of the spectrum (1020-1080 nm), which is the region of interest for background absorption, the resonant absorption abruptly decreases as the temperature lowers, reducing significantly the magnitude of pump-induced temperature changes. Signal to noise ratio should be maximized increasing the pump power (not readily available in this spectral region), but also operating on the thermal stability of the sample.

Moreover, in order to avoid alteration of the heat capacity of the sample, high-sensitivity and non-contact temperature measurements operating a low temperature must be used. Thermal cameras, usually employed for room temperature LITMoS test, for examples, can no longer be used. A special version of differential luminescence thermometry, which uses the PL spectra produced by a continuous excitation with a probe laser, will be set up to achieve the necessary sensitivity.

A schematic of the final experimental setup is shown in **Fig. 1**. As can be seen from the schematic in **Fig.1b**, the sample is clamped to a copper cold-finger inside a cryostat, attached to a closed-cycle He refrigerator, also equipped with heater coil. The tricky point here is the use of high-purity glass slides, in between the sample and the holder, to provide a tunable thermal resistance between the sample and the cold-finger structure. The thickness of the glass is determining for the time-scale of the system and needs to be optimized in advance. A silicon diode sensor (TS 1), integrated with the PID controller, is attached to the cold-finger to control its temperature, and a second sensor (TS 2) is used to monitor the temperature of the Aluminum clamp, where the sample is mounted.

For sensitive measurements of temperatures changes, a time-gated version of differential luminescence thermometry (DLT) has been set up. In this method, once the sample is cooled down to a given temperature, where it can be kept stable within 0.1 K, pump-induced temperature changes can be measured from variations in PL spectra produced by a 1020 nm probe laser, continuously exciting the sample (**Fig. 1a**). High stability of sample temperature and probe power are essential for accurate measurements. Three different pumping sources have been used to cover the entire spectral region with sufficient high pump power: a tunable Ti:Sapphire laser operating between 940 and 1070 nm with ~ 2 W output power, a VECSEL emitting ~ 2-5 W between 1010 and 1030 nm and a 1070 nm

fiber laser with up to 400 W of output power. The excitation time needed is function of the thermal resistance between the cold-finger and the sample.

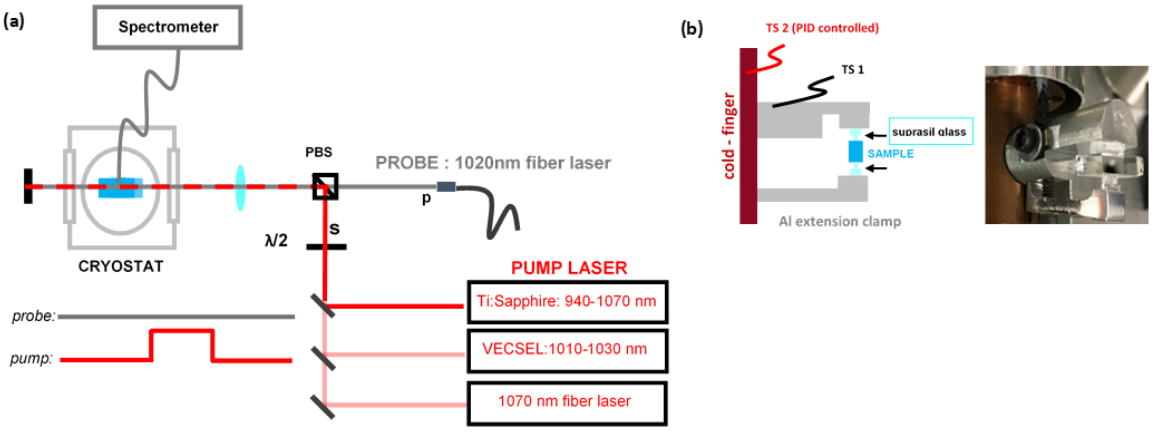

Fig.1: (a) Experimental setup for low-temperature LITMoS test (CAN BE REPLACED with Fig.4 from Mansoor`s manuscript). (b) Schematic and picture of sample mounting.

Using this set-up, after fine tuning of multiple parameters, we have been able to perform first LITMoS tests below room temperature. Temperatures down to 150 K have been explored providing experimental evidence of a temperature dependence of background absorption for this Yb-Tm sample. Results are shown in **Fig. 2a**, where red dots represent experimental data and the black line represents a Boltzmann-type fit to data. **In Fig. 3** experimental data, along with fitting model curves, of LITMoS tests performed at room temperature and 150 K are reported. On the same plot, the dashed curve represents the cooling efficiency at 150 K, in the approximation of constant background absorption, showing the difference which is neglected when considering α_b as temperature independent.

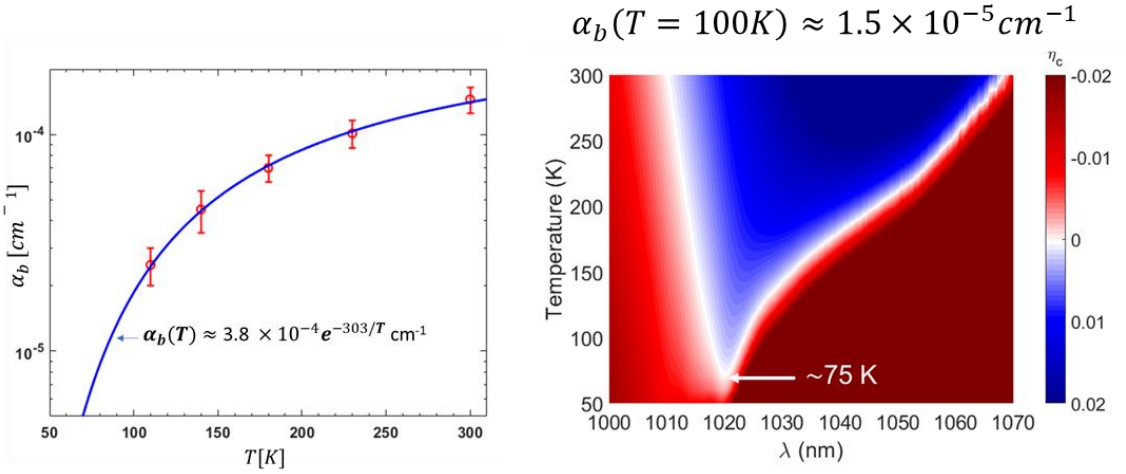

Fig. 1: (a) Experimental data points of background absorption (red dots) vs temperature for YLF:5%Yb, co-doped with Tm (0.0016%), along with extrapolated Boltzmann-type model (black line). (b) 2D plot of cooling efficiency vs wavelength and temperature

calculated with temperature-dependent background absorption (Boltzmann-type fit shown in Fig.2a). Blue (red) regions indicates cooling (heating). The white transition line represents the spectrum of the MAT (Minimum Achievable Temperature); a global MAT (gMAT) of ~75 K can be estimated for excitation around 1020nm.

If, for this sample, background absorption decreases as a function of temperature following the Boltzmann-type fitting function represented in **Fig.2a,** a MAT below 80 K can be predicted; consistent with results of power cooling experiments, and able to explain the unexpected achievement. The 2D plot showing cooling efficiency vs wavelength and temperature with temperature-dependent background absorption is shown in **Fig.2b**.
At this point, the question we still need to answer is why the background absorption would be temperature dependence and how universal this behavior is. Previous experiments conducted on YLF:Yb samples showed a severe impact of divalent transition metals, and especially Fe^{2+}, on the background absorption [1]. As for rare earths, also for other kinds of impurities, such as transition metals, the phonon broadening is expected to significantly shrink the electronic absorption lines as the temperature decreases. Conversely to rare-earths, however, transition metals show much broader absorption bands: in the `lucky` coincidence in which the cooling excitation region of Yb-doped fluorides is located outside the electronic resonance region, the absorption of impurities will decrease as the temperature goes down. Absorption and emission spectra of transition metals are also strongly dependent on the host material and literature data are not readily available for fluoride single crystals. This hole provides us one more reason to directly investigate the synthesis process. In addition to investigating purification techniques and reproducibility of growth parameters, finding a convenient crystal growth would allow us to grow samples with intentional doping of suspicious transition metals (and other impurities) to directly investigate their spectroscopic properties in YLF crystals, along with temperature dependences, developing a knowledge which cannot be readily found in literature, and would also be applicable to other fields highly sensitivity to low levels of impurities.

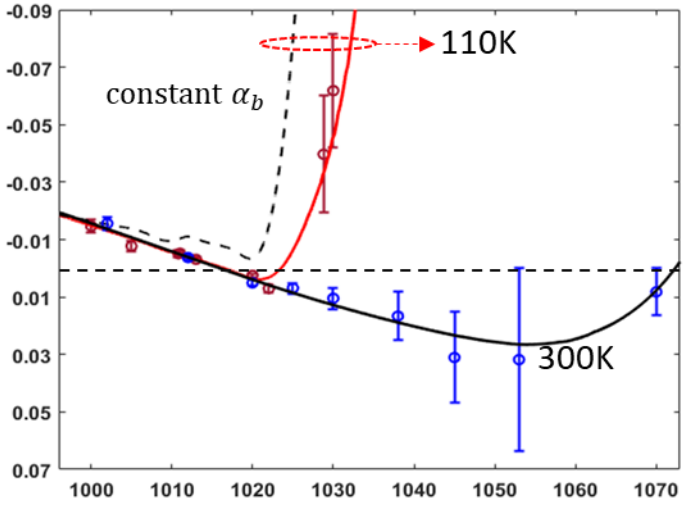

Fig.3: Experimental data points and fitting model curve of cooling efficiency for YLF:5%Yb co-doped with Tm (0.0016%) measured at 300 K (red) and 150 K (blue). The blue dash curve shows the cooling efficiency at 150 K in the approximation of temperature independent background absorption.

c. Progress in Bridgeman Crystal Growth

Extremely stringent requirements at the material level need to be met for laser cooling materials, in terms of both crystal quality and optical purity. Impurities incorporated even at very low levels, ppm (parts per million) or below, can readily offset the laser-induced cooling process, via exothermic non-radiative quenching or background absorption processes, leading to net heating or inefficient cooling performances. So far, by using exquisitely high-quality Yb-doped YLF single crystals, cryogenic and even sub-100K temperatures have been reached, and further improvements of current purity levels appear the key point to reach even lower temperatures (in the 70-80 K range) with greater efficiencies. However, a large sample-to-sample variability in cooling performances is being observed: samples with same nominal composition, apparently grown under identical conditions and showing equivalent crystal and optical quality, present very different laser cooling performances, ranging from samples cooling to sub-100K temperatures, that look like "rare events", up to samples showing net heating. This big elephant in the room is still puzzling and limiting progress not only in fundamental material-level studies but also in the engineering of this technology for use in a variety of applications.

A systematic study at the material level becomes essential for both understanding sources of losses and uncertainty and improving the current material performances. Both these necessities motivated us to directly investigate the synthesis process-line, involving purification processes for raw materials and the actual sample growth, which determines both final purity and structural quality. This research is being conducted by setting up a vertical Bridgman growth system, in collaboration with LANL.

To date, laser cooling crystals have been basically produced by using the Czochralski technique (**Fig.1a**). This method typically requires large batches of raw materials for bulk growth (~ tens of grams) and cooling-grade reproducibility has not been easily achieved yet.

In view of a systematic study of growth parameters and impurities effect, the Bridgman method presents several advantages (**Fig.1b**). Firstly, it allows for the growth of bulk crystals on the few gram scale, which is compatible with purification techniques (such as electrochemical purification, 2nd progress report). Production rates are much faster, allowing systematic testing of a much wider range of parameters. Chamber components (crucible, heat shields, …), mostly machinable at UNM, can be better replaced, making this technique more suitable for investigation of impurity-mediated processes, by growing samples with intentional doping of "suspicious'' elements, like transition metals, whose spectra are strongly dependent on the host materials and spectroscopic data for fluoride single-crystals are not readily available in literature. This understanding, if developed,

could then be applied back to the Czochralski method. A twofold aim is thus pursued: developing an on-site crystal growth system for production of cooling-grade samples and a fundamental study of spectroscopic data not available in literature and applicable to many other fields sensitive to low-levels of impurities (such as transition metals). Also, the Bridgman growth results in a more standard procedure which can be better automated, reducing the variability in potentially uncontrollable growth parameters.

An existing micro-pulling down furnace at LANL has been reconfigured for Bridgman growth, which is shown **Fig.2** along with a schematic of its interior. The furnace features RF heating and a high-precision translation stage for fine controlled movements (0.2-2 mm/h), with minimal vibrations under vacuum or elevated pressures. The crucible, placed in the middle of the RF coil, is moved downward along a negative temperature gradient. A suitable thermal profile is required to induce controlled crystallization of the melt from the bottom of the crucible upwards. A high vacuum system is used to evacuate the chamber to low pressure, before the growth, removing oxygen and water residues to minimize undesired reactions with the fluoride melt at high temperatures. The growth process is usually performed in high-purity argon overpressure to minimize evaporative losses.

When setting up a new growth procedure, a variety of parameters needs to be optimized to first identify suitable conditions for the growth of a single-crystal.

First tests resulted in mostly polycrystalline materials, as shown in **Fig.3a and 3b**. A glassy carbon crucible depicted in **Fig.3c** was used at this stage. One of the main issue at that point was the missing tip section, resulting in improper seeding at the starting point, favoring more a polycrystalline nucleation than a single-crystal formation. Black foreign particles were also incorporated into the melt, and they likely acted as spurious nucleation centers as well.

Modifications of crucible shape resulted in remarkable improvements of crystal quality. Due to the characteristic skin heating provided by the RF coil, switching from type 1 (glassy-carbon crucible type shown in Fig.3c) to type 2 crucible (**Fig.4a**), the latter machined out of a single block of graphite rod, has resulted in more favorable longitudinal thermal gradient along the crucible. **Fig.4b** shows an undoped LLF sample grown in a type 2 crucible: the sample resulted mostly in a single crystal, with black foreign residues principally deposited on the surface. This result provides a first experimental demonstration of small-scale Bridgman growth of fluoride single crystals.

Subsequent investigation mainly focused on YLF crystals, in order to both identify cooling-grade conditions but also investigate impurities-mediated processes via intentional doping with the most suspicious sources of background absorption in YLF:Yb sample investigated for laser-cooling, i.e. transition metals. Compared to LLF, however, the YLF crystal has incongruent melting behavior [1], making the growth of high-quality samples much more difficult, especially in the Bridgman system. The incongruent melting behavior of YLF requires, as starting point for the growth, a non-stoichiometric mixture of the two components (LiF, YF_3) in order to avoid precipitation of YF_3 upon cooling the melt during the growth process. In order to combine the two goals, YLF samples with slight Fe^{2+} doping (1%) have been grown. Exploring different points of the composition space, and growth rates, progressive improvements in crystal quality have been observed. As can be seen from

Fig.5, starting from the minimum LiF excess (52.5%) required to achieve the phase-transition between homogenous liquid and YLF crystal, and increasing that parameter (up to 60%) while reducing the translation rate of the crucible, clear single-crystal regions can be observed (**Fig.5b**), although polycrystalline structures still dominate most of the volume of the crystal. These structures emerge from the seed channel section of the crucible, where the necessary mixing of the components is probably not efficient, and propagates, outwards from the center, along the growth axis, up to reach the eutectic composition at the end of the growth, where the eutectic solidifies. Clear regions of this sample will be polished and used to try to measure the absorption of Fe^{2+} in YLF.
Future developments for YLF growth will involve further changes in the composition space and crucible shape, to better favor mixing of the two components. Powder X-ray diffraction will be used to investigate the nature of the polycrystalline microstructures observed. Other than YLF, efforts will also focus on doped LLF and similar fluorides.

[1] *R. E. Thoma et al., PHASE EQUILIBRIA IN THE SYSTEM LiFYF3. J. Phys. Chem., 65 (1961) 1961.*

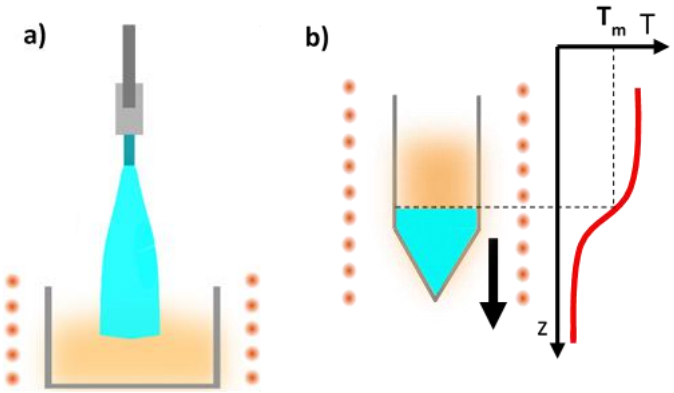

Fig.1: a) Principle of Czochralski growth: A single-crystal is grown from the liquid phase, pulling up, while rotating, a crystal-seed dipped into the melt to induce controlled nucleation. b) Principle of Bridgman growth: A single-crystal is grown translating the crucible, where the molten material is contained in a properly shaped negative thermal gradient.

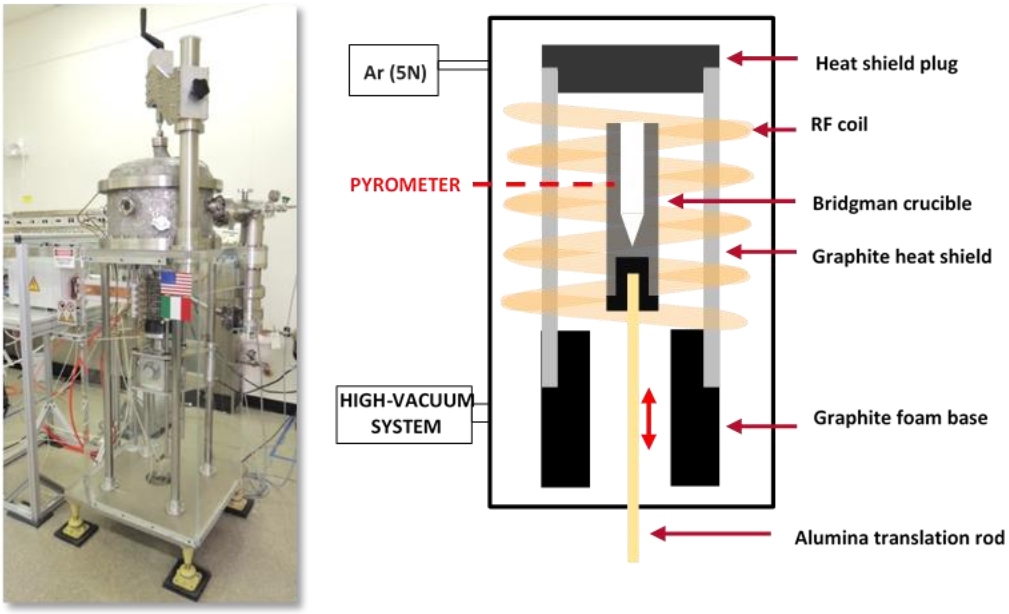

Fig.2: Picture (a) and internal schematic (B) of the Bridgman reconfigured furnace at LANL.

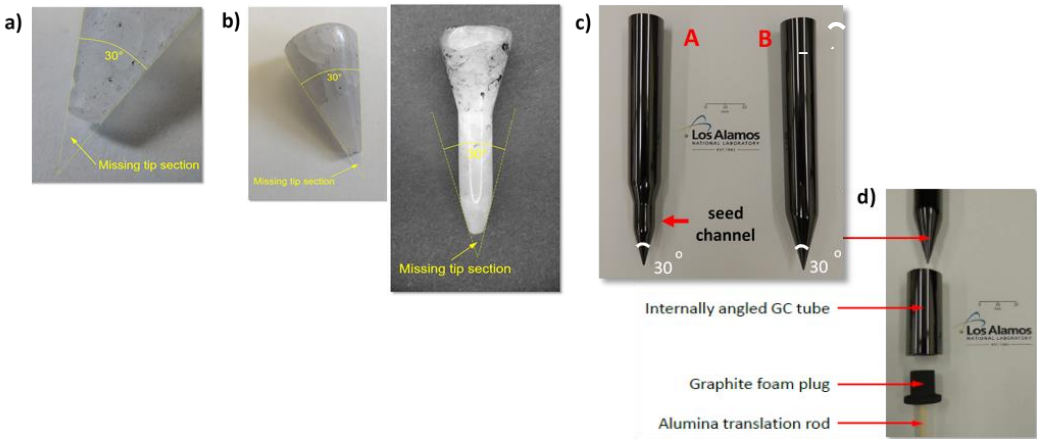

Fig.3: YLF:10%Yb (a) and undoped LLF (b) samples grown in type A and B glassy-carbon crucibles, shown in (c). Mounting of crucibles A and B.

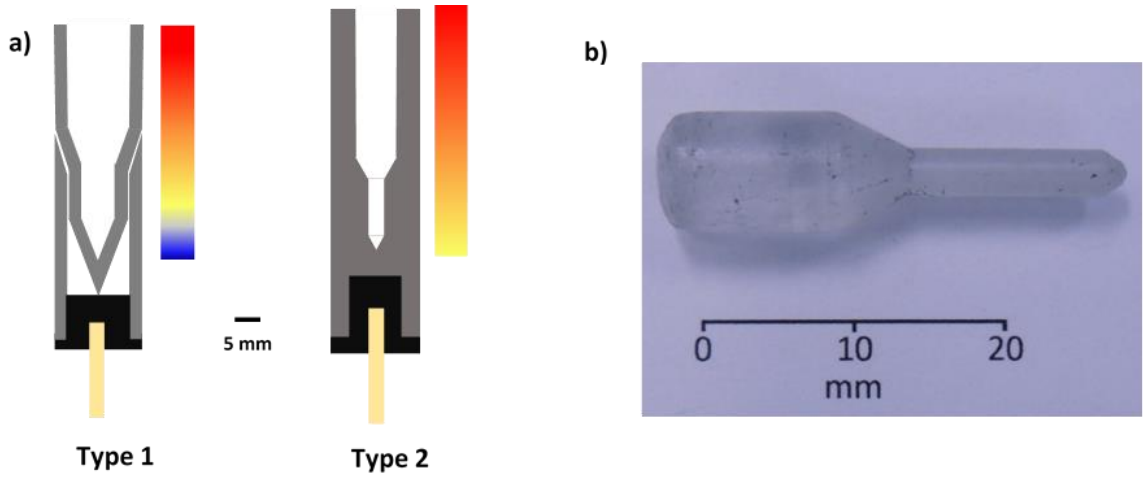

Fig.4: a) Schematic of glassy-carbon crucibles (shown in Fig.3c, referred to as type 1, and second generation (type 2) of Bridgman crucibles, machined from isostatic graphite rods. The color map provides indication of the longitudinal thermal gradient along the crucible. b) Undoped LLF in type 2 graphite crucible.

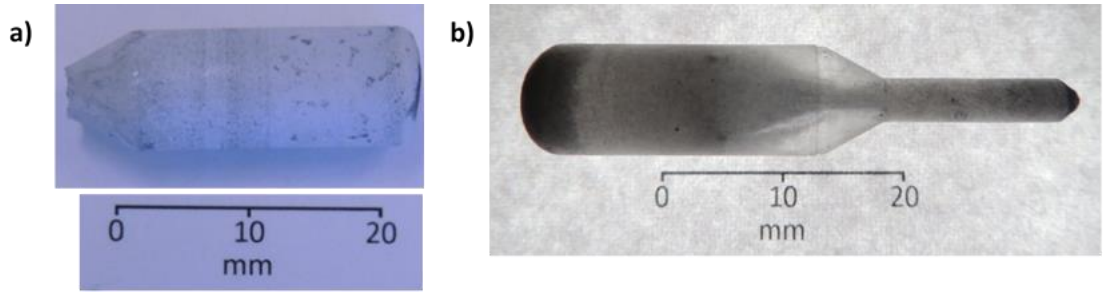

Fig.5: YLF:1%FeF2 grown in type 2 crucibles with: (a) composition LiF:YF3=52.5:47.5 and translation rate 0.8 mm/h, (b) composition LiF:YF3=60:40 and translation rate 0.4 mm/h. Increasing the LiF excess, slower pulling rate is desirable for good phase separation of LiF and YLF.

- **Energy-Gap Scaling:** ***Looking beyond Yb^{3+}***

Optical refrigeration of 1% and 2%Tm:YLF crystals

Looking for more efficient cooling crystals, we investigated optical refrigeration in mid-IR in Tm and Ho doped crystals. As shown in Fig. A16, we have designed and constructed a MgO:PPLN based mid-IR continuous wave optical parametric oscillator (CW-OPO) tunable from 1730 nm-2800 nm (1730-2100 nm for signal and 2200-2800 nm for idler) to investigate optical refrigeration in Tm and Ho doped crystals. The OPO is pumped with a 1070 nm fiber laser and the PPLN is temperature tuned from 23°C to 200°C to provide required output beams for laser cooling experiments. Fig. A16(c) shows the narrow linewidth (<1 nm) OPO outputs which are used for LITMoS tests on Tm and Ho doped samples.

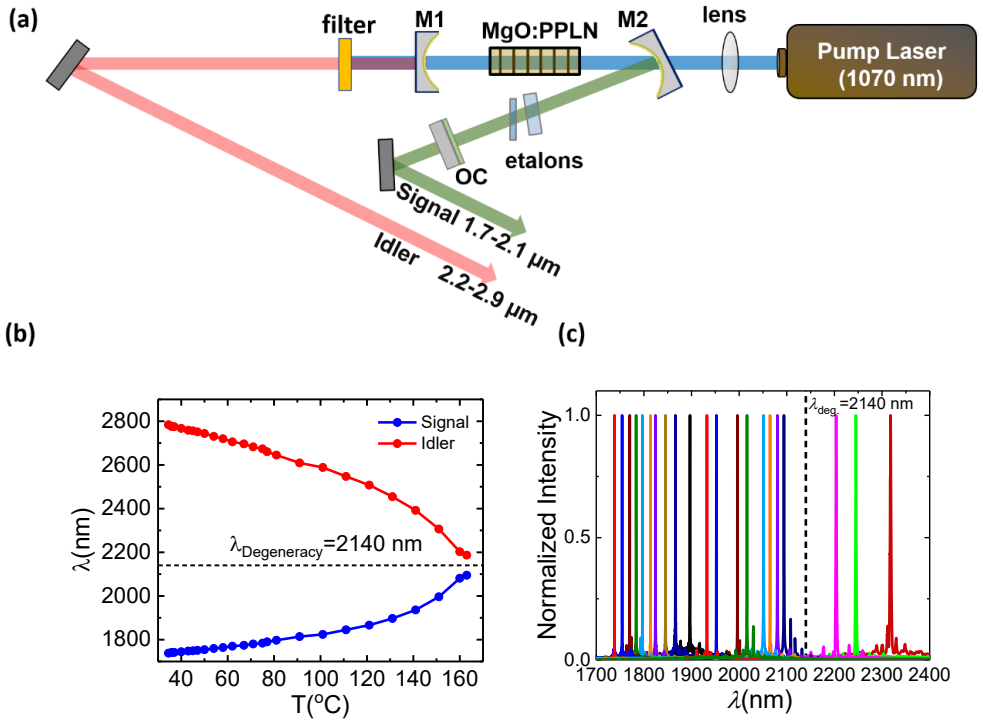

Figure A16*: (a)Schematic of CW-OPO setup, (b) phase matching curve of MgO:PPLN as temperature of oven varies from 30-160°C, (c) narrow linewidth (<1 nm) OPO outputs.*

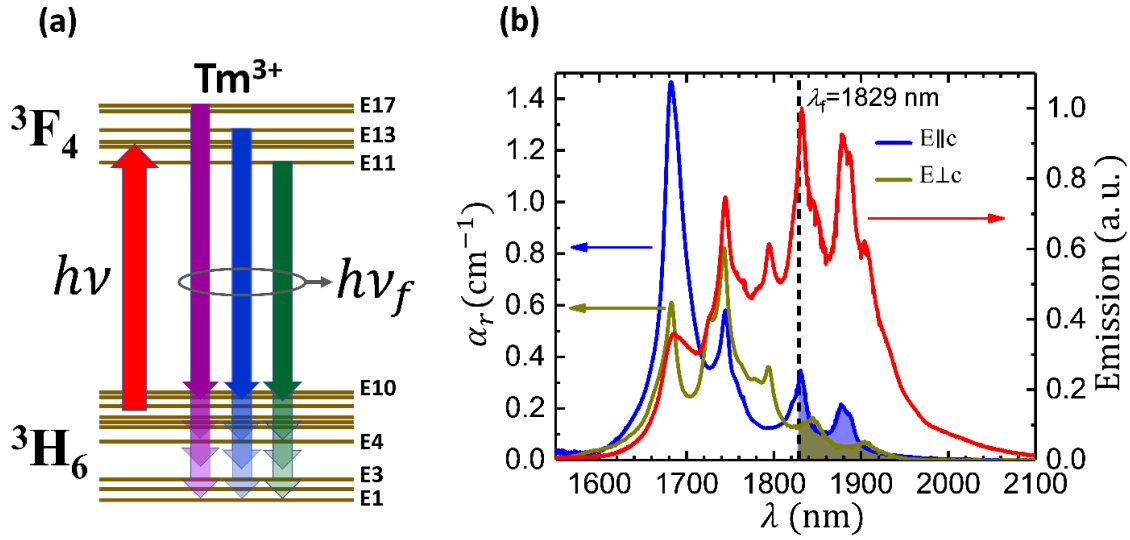

***Figure A17**: (a) Anti-stokes florescence cooling process in Tm:YLF crystal, (b) emission and absorption (E∥c and E⊥c) spectra for 2% Tm:YLF crystal with the cooling tails above mean emission wavelength λ_f=1829 nm for each polarization.*

Anti-stokes fluorescence cooling in Tm:YLF crystal involves the ground state manifold ($^3H_6$) and the first excited state manifold ($^3F_4$), and the cooling process happens within the shaded region in Fig. A17 (b) under the absorption spectrums (cooling tail) while the crystal is excited with a laser at $\lambda>\lambda_f$ where λ_f denotes the mean fluorescence wavelength of crystals. In Fig. A17 (b), the emission spectrum of 2% Tm:YLF crystal is measured with Thorlabs OSA203B and the absorption spectrums are measured directly with an FTIR device. λ_f=1829 nm for 2% Tm:YLF is obtained via averaging over two polarized (E∥c and E⊥c) emission spectrums. To investigate if the sample is of "cooling grade" and quantify its external quantum efficiency (η_{ext} or EQE) and background absorption (α_b), the sample needs to be excited with a tunable coherent source within the cooling tails. As explained above, we have used a home-made mid-IR CW-OPO to investigate mid-IR optical refrigeration in Tm and Ho doped crystals.

We used high purity 2.4×3.0×3.2 mm^3 1% Tm:YLF (University of Pisa, Italy) and 4.8×4.8×5.0 mm^3 2% Tm:YLF (AC Materials, Tarpon Springs, FL) crystals grown by Czochralski process in the experiments.

The cooling efficiency η_c of 1% and 2% Tm:YLF crystals are measured at room temperature via LITMoS tests as shown schematically in Fig. A18 (a). $\eta_c(\lambda) = \Delta T/KP_{abs}$ is evaluated by measuring ΔT and the absorbed power while sample is excited with the OPO signal (λ) from below to above λ_f, and K is a constant (scaling factor) that varies inversely with the thermal load on the sample. ΔT is extracted from processing of thermal images captured by calibrated Thermal Eye Nanocore 640 camera (L3-Communications Corporation, TX, USA) and P_{abs} is calculated form the OPO output power residue and absorption coefficients of the samples at each wavelength considering Fresnel reflection corrections.

The temperature and wavelength dependent cooling efficiency of a solid-sate material is written as follows;

$$\eta_c(\lambda,T) = 1 - \eta_{ext}\eta_{abs}(\lambda,T)\frac{\lambda}{\lambda_f(T)}$$

where $\eta_{abs} = 1/(1+\alpha_b/\alpha_r(\lambda,T))$, η_{ext} and $\lambda_f(T)$ are absorption efficiency, external quantum efficiency (EQE) and temperature dependent mean emission wavelength of the sample respectively, and λ is the wavelength of the pump laser. In absorption efficiency η_{abs} relation, $\alpha_r(\lambda,T)$ and α_b are resonant absorption and background absorption coefficients of the sample.

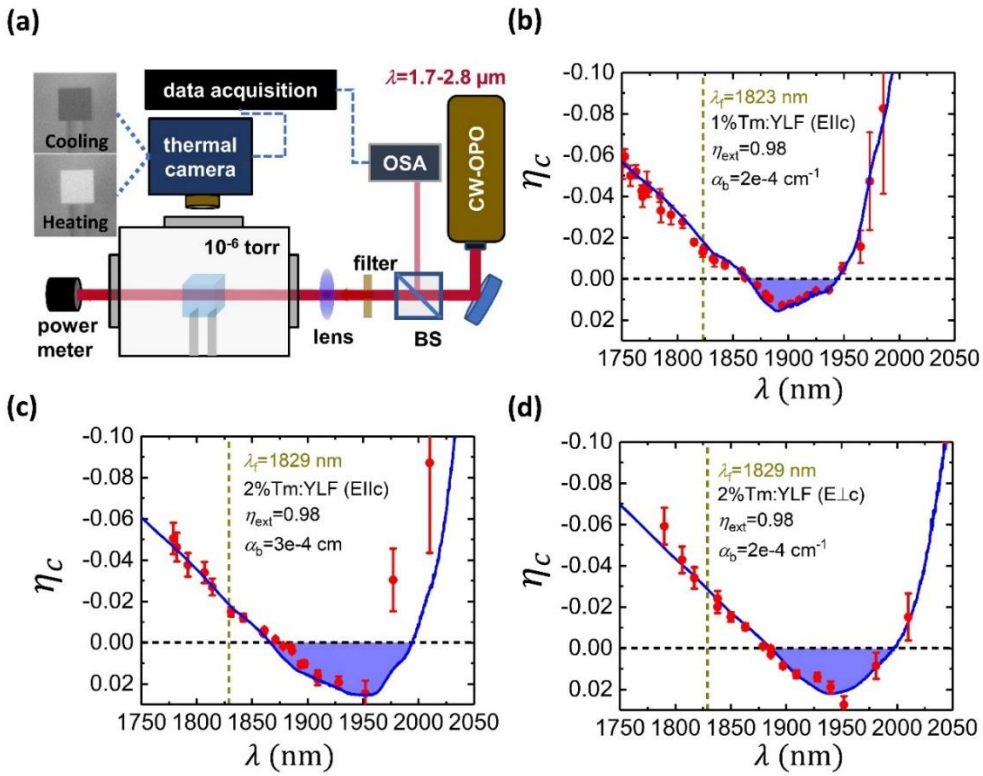

***Figure A18**: (a) schematic of experimental setup for LITMoS tests, and cooling efficiency of (b) 1% Tm:YLF (E∥c), (c) 2%Tm:YLF (E∥c) and (d) 2%Tm:YLF (E⊥c)crystals.*

Once $\eta_c(\lambda,T)$ is evaluated at T=300 K, external quantum efficiency η_{ext} and background absorption α_b are obtained from the best fit to $\eta_c(\lambda,T)$ equation. Figures A18 (b)-(d) show the LITMoS test results for 1% Tm:YLF and 2% Tm:YLF samples in E∥c and E⊥c pump polarization configurations (c is the optical axis of the crystal). Table A1 summarizes η_{ext}, α_b, and crossing wavelength λ_c (transition from heating to cooling) for 1% and 2% Tm:YLF:

Sample	Pol.	η_{ext}(%)	α_b(cm^{-1})	λ_c(nm)
1% Tm:YLF	E∥c	98.0±0.2	(2±1)e-4	1861±1
2% Tm:YLF	E∥c	98.2±0.3	(3±1)e-4	1869±1
2% Tm:YLF	E⊥c	98.0±0.3	(2±1)e-4	1879±2

***Table A1**: Summary of Tm:YLF sample parameters.*

A figure of merit for any cooling-grade material is its so-called minimum achievable temperature (MAT) which defines the lowest temperature at which η_c vanishes and subsequently turns negative (i.e. enters the heating regime). MAT is very important factor for optical cryocooler applications since the goal is to achieve the lowest possible temperatures. To estimate the MAT for any cooling grade crystal, one needs to examine the constituents of η_c namely $\lambda_f(T)$ and $\alpha_r(\lambda, T)$ at low temperatures assuming that η_{ext}, α_b are temperature independent. $\lambda_f(T)$ is measured by recording the fluorescence spectra $S(\lambda)$ associated with $^3H_6$ to $^3F_4$ transition as the temperature of the sample, placed in a cryostat, is varied from 300 K to 80 K. The emission spectra are collected by a fiber-coupled mid-IR optical spectrum analyzer (Thorlabs OSA203B). $\lambda_f(T)$ is calculated by performing a weighted average on E∥c and E⊥c polarized $S(\lambda)$ at each temperature. Figure A19 (a) shows $\lambda_f(T)$ for 1% and 2% Tm:YLF samples from 300 K to 80 K. $\lambda_f(T)$ for 2% doped sample is around 9 nm longer due to the stronger reabsorption effect at higher doping levels; however, both crystals show ~3.2% shift in $\lambda_f(T)$ value from 300 K to 80 K.
The next task to create MAT curves is measuring $\alpha_r(\lambda, T)$. Temperature-dependent resonant absorption coefficients $\alpha_r(\lambda, T)$ are extracted from reciprocity theorem using polarized emission spectra at each temperature. Proportional spectra obtained from reciprocity is calibrated to a directly measured absorption value (e.g. at λ=1830 nm) to get the exact absorption spectra $\alpha_r(\lambda, T)$ at each temperature. The calibrated absorption spectra from reciprocity exhibit less noise in the long wavelength tail (λ>1870 nm), which is of particular interest for laser cooling and RBLs. Figure A19 (b) shows $\alpha_r(\lambda, T)$ for 1% Tm:YLF crystal from 300 K to 80 K in 20 K increments.

Knowing η_{ext}, α_b, $\lambda_f(T)$, and $\alpha_r(\lambda, T)$, plot of $\eta_c(\lambda, T)$ identifies the cooling and heating spectral regimes at all temperatures, and subsequently shows the global MAT and its pumping wavelength for the crystal. Figures A19 (c) and (d) illustrate MAT plots for 1% Tm:YLF (E∥c) and 2% Tm:YLF (E⊥c) respectively. The white demarcation in these plots signifies η_c= 0 and marks the MATs for the corresponding excitation wavelengths. The shown global MATs are 190±10 K at 1888 nm for 1% Tm:YLF (E∥c) and 160±10 K at 1910 nm for 2% Tm:YLF (E⊥c) which correspond respectively to E5-E11 and E8-E11 transitions between $^3H_6$ and $^3F_4$ manifolds in Tm^{3+}-doped YLF. It is also worth noting that these wavelengths coincide with readily available high-power Tm (fiber) lasers especially for 2% Tm:YLF in E⊥c configuration. Moreover, new investigations on background absorption of Yb:YLF crystal shows that α_b also drops as temperature decreases which means the real global MATs are even lower than estimated values in Fig. A19 (c) and (d).

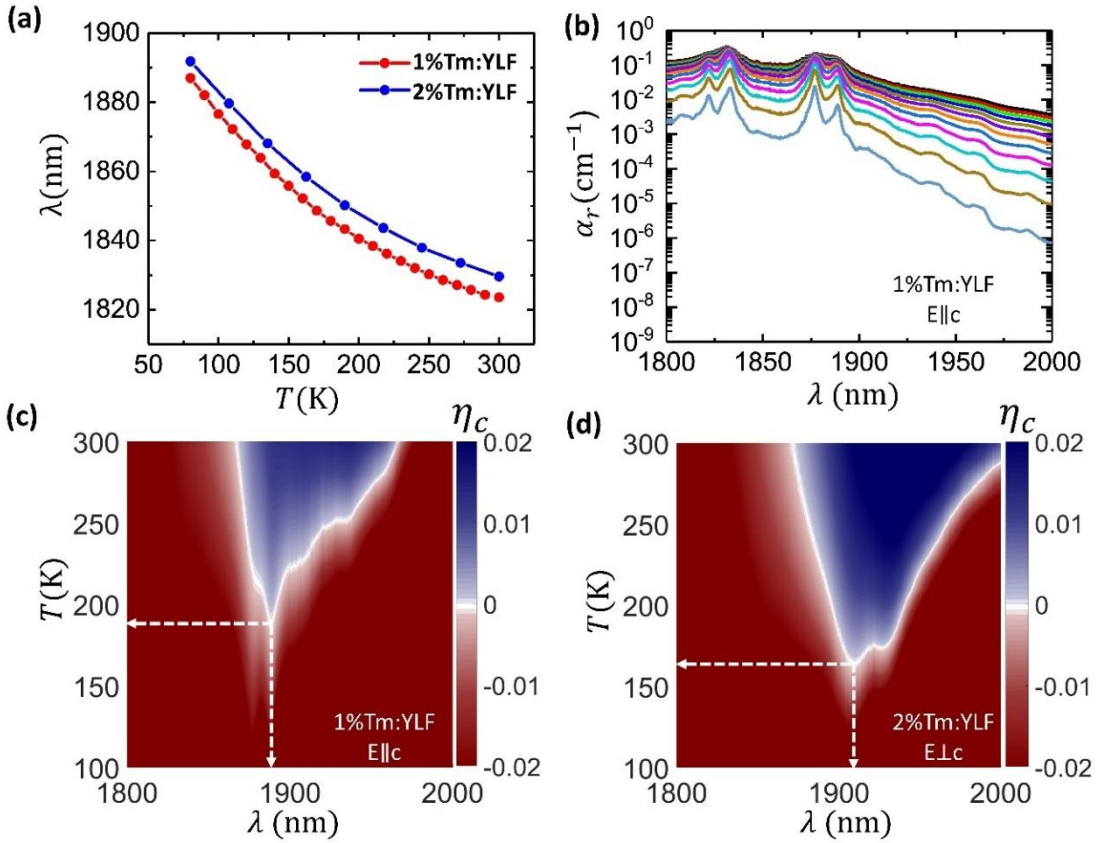

Figure A19: *(a) Temperature dependent mean emission wavelength $\lambda_f(T)$ of 1% and 2% Tm:YLF crystals, (b) Temperature dependent resonant absorption coefficient $\alpha_r(\lambda, T)$ of 1% Tm:YLF crystal, (c) MAT curves for (c) 1% Tm:YLF (E∥c) and (d) 2% Tm:YLF (E⊥c).*

Considering temperature dependence of α_b and (or) assuming improved growth process to have purer Tm:YLF crystals, feasible estimations for global MATs of 2% Tm:YLF crystal with back ground absorption of α_b=1e-5 cm^{-1} are 120±10 K for E∥c and 110±10 K for E⊥c as depicted in Fig. A20 (a) and (b) respectively. Such estimated low MATs show the great potential of Tm:YLF crystals toward developing mid-IR optical cryocoolers. It is also notable that mid-IR optical coolers based on Tm and Ho doped crystals can potentially be thermal-link and cold-finger free to integrate into certain devices which are transparent in mid-IR like NIST single-crystal Si reference cavity.

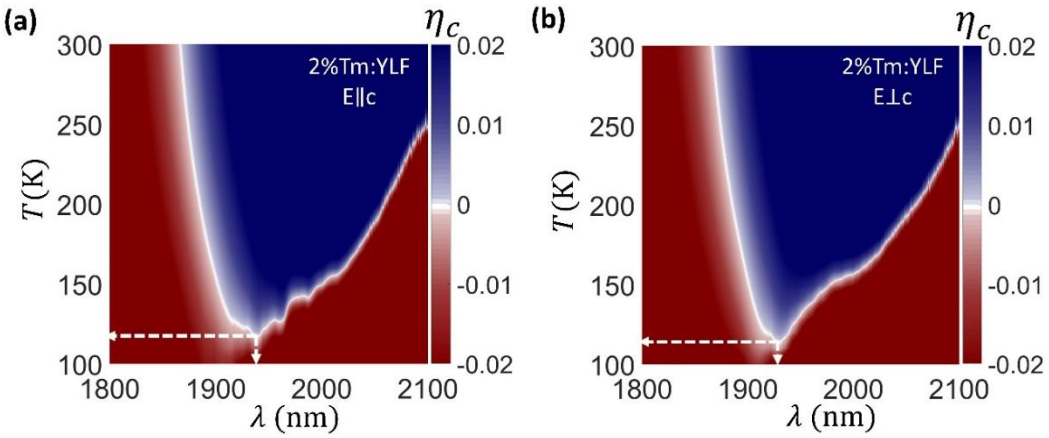

***Figure A20**: Estimated MAT of 2% Tm:YLF assuming α_b=1e-5 cm^{-1} for (a) E∥c and (b) E⊥c polarizations.*

Optical refrigeration of 1% Tm:BYF crystal

Further investigations on laser cooling of Tm-doped crystals result is observation and characterization of optical refrigeration in 1% Tm:BYF crystal. BYF is a biaxial host material which has lower phonon energies compared to YLF, so multi-phonon relaxations can be completely suppressed in such host material and it turn into having extremely high EQE. Figures A21 (a) and (b) show the LITMoS test results for 1% Tm:BYF in two different pumping polarizations E||b and E||c. The results show that 1%Tm:BYF has very high EQE (0.999 for E||b with α_b=2.5e-4 cm^{-1} and 0.997 for E||c with α_b=1.0e-4 cm^{-1}) which is very important for mid-IR RBL and optical cryocooler applications.

Following the recipe described for Tm:YLF crystals, performing low-temperature analysis on the sample, provide us with MAT curves of 1% Tm:BYF sample. Figure A22 shows the results of low temperature analysis for this sample. The temperature dependent mean emission wavelength redshifts ~3.6% starting from 1814 nm at T=300K as shown in figure A22 (a). The temperature dependent resonant absorption coefficients for E||b polarization is shows in Fig. A22 (b). Plugging low temperature results into $\eta_c(\lambda, T)$, gives us the Mat curves for different polarizations. Global MATs for 1% Tm:BYF sample are 160 K at 1860 nm for E||b and 160 K at 1855 and 1926 nm for E||c polarizations as depicted in Fig A22 (c) and (d). Since the sample has extremely high EQE, the MAT could be further improved via increasing the doping concentration of lowering the background absorption. An order of magnitude decrease in background absorption would result in MATs of 120 K at 1923 nm and 110 K at 1926 nm for E||b and E||c respectively as shown in Fig. A23 (a) and (b). It is notable that high power lasers at these wavelengths are readily available compared with MAT points at higher background absorption; however, since the MAT points are shifting toward longer wavelengths due to availability of higher cooling efficiencies at those wavelengths, a good idea to catch those wavelengths for any sample is to develop a Tm-fiber amplifier seeded with a mid-IR CW-OPO which it high power and tunable in desired range. MAT points around 1860 nm could be improved by increasing the dopant concertation of Tm ions.

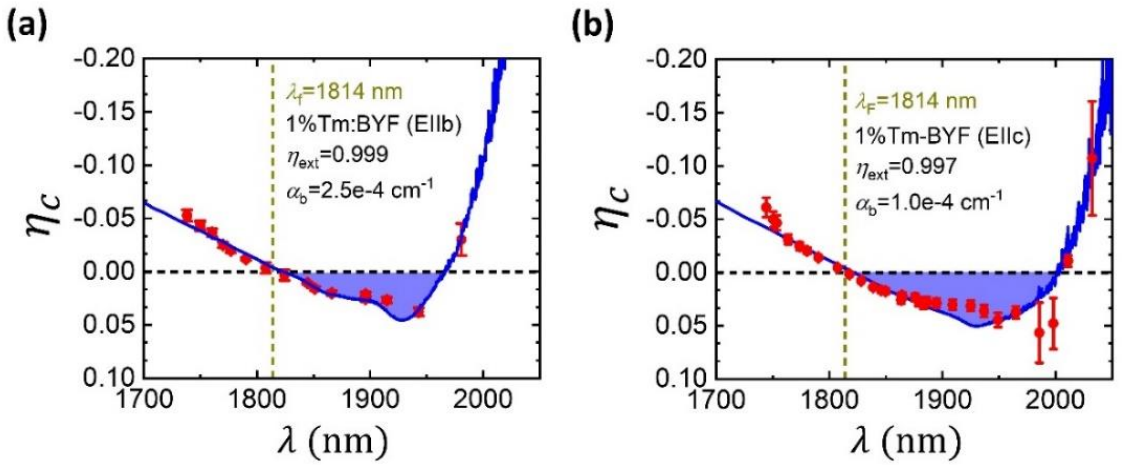

Figure A21*: Cooling efficiency of 1%Tm:BYF crystal for (a)* E||b *and (b)* E||c polarizations.

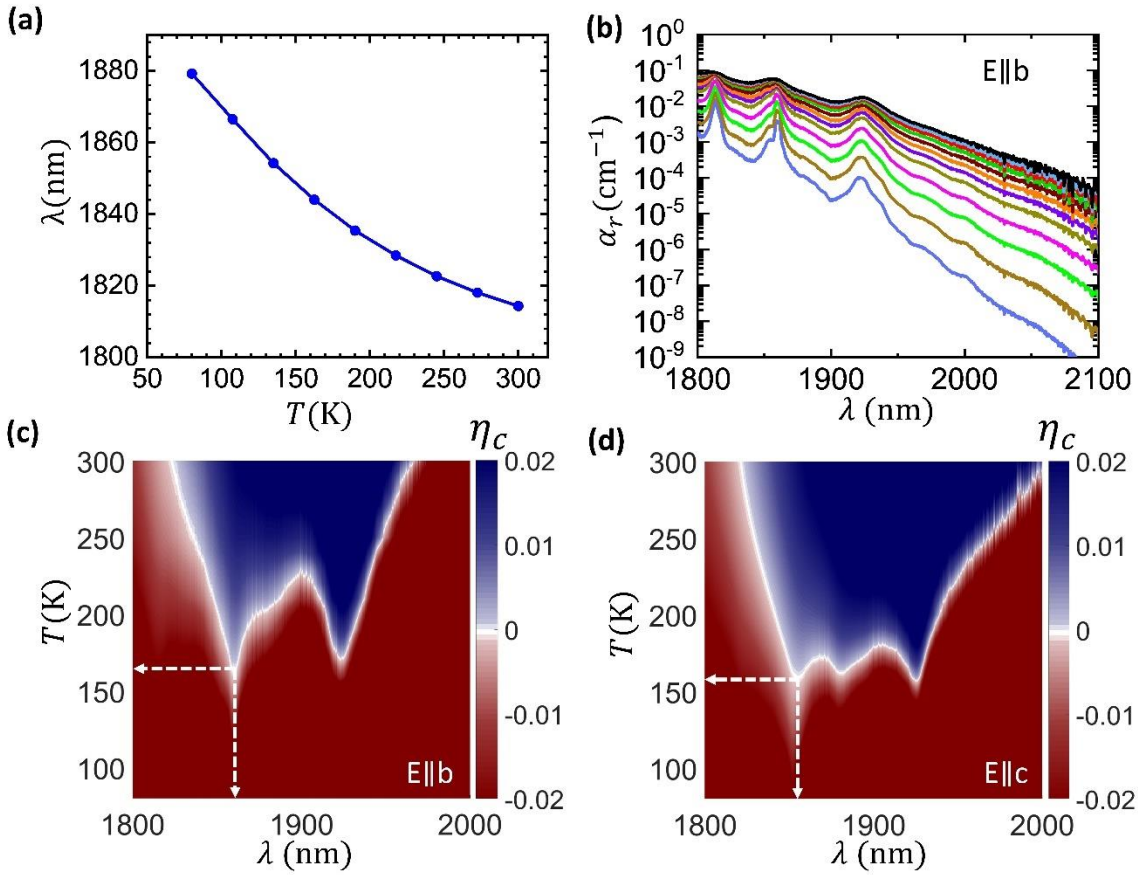

Figure A22: *(a) Temperature dependent mean emission wavelength $\lambda_f(T)$, (b) Temperature dependent resonant absorption coefficient $\alpha_r(\lambda, T)$ in E//b polarization and (c) MAT curves for (c) E//b and (d) E//c of 1%Tm:BYF crystal.*

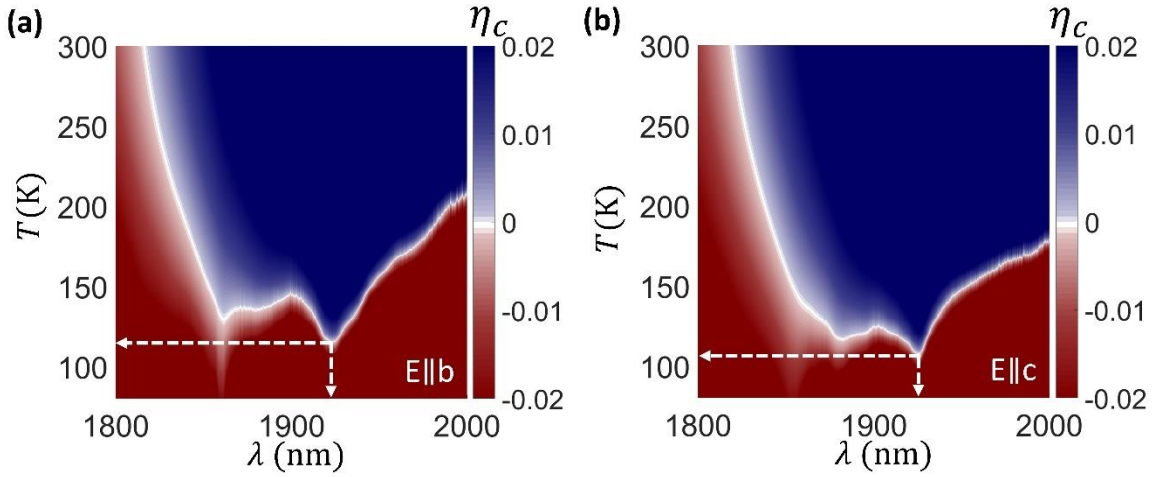

***Figure A23**: Estimated MAT of 1%Tm:BYF with (a) α_b=2.5e-5 cm^{-1} for E∥b and (b) α_b=1.0e-5 cm^{-1} for E∥c polarizations.*

Optical refrigeration of 1% Ho:YLF crystal

Looking for more efficient cooling materials in mid-IR, we observed optical refrigeration in 1% Ho:YLF crystal. We used a 4.8×4.8×5.0 mm^3 high purity 1% Ho^{3+}-doped YLF crystal grown by Czochralski process (AC Materials, Tarpon Springs, FL). The measured room temperature absorption coefficient and emission spectra associated with the transitions between the ground-state ($^5I_8$) and the first excited state ($^5I_7$) Stark manifolds are shown in Fig. A24. The shaded area in the absorption spectrum is the so-called "cooling tail" with $\lambda>\lambda_f$, where λ_f=c/ν_f~ 2015 nm denotes the mean fluorescence wavelength.

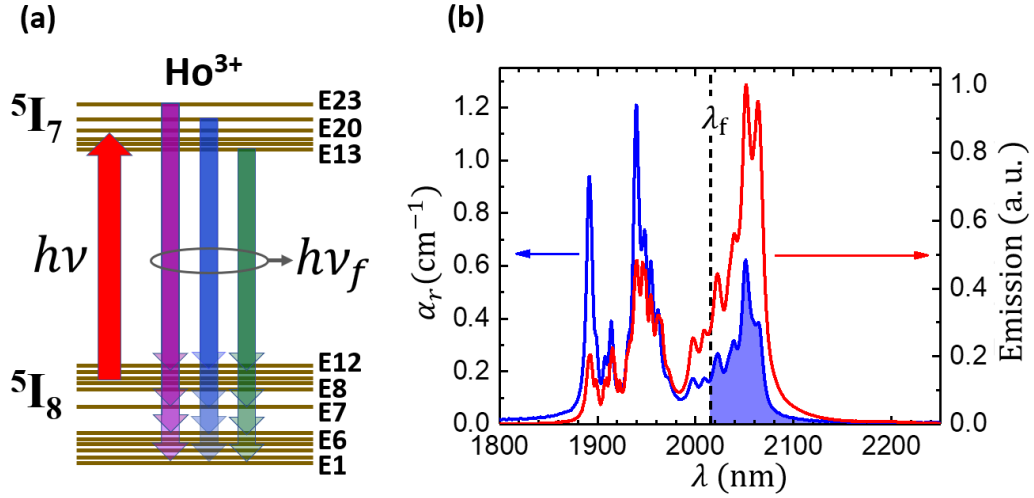

***Figure A24**: (a) Anti-Stokes fluorescence cooling process in Ho^{+3} ions, (b) emission (red) and absorption (blue) spectra of 1% Ho:YLF at T=300 K ($\lambda = c/\nu$). The shaded region denotes the cooling tail ($\lambda > \lambda_f$=2015 nm). Emission spectrum measured with a scanning optical spectrum analyzer under excitation at 1890 nm; absorption spectrum is directly measured with an FTIR spectrometer under E∥c configuration.*

Cooling efficiency of 1% Ho:YLF sample has been evaluated using our home-made CW-OPO as shown in Fig. A25 (a). η_{ext}=0.98 and α_b=5e-5 cm^{-1} are obtained for this sample

as illustrated in Fig. A25 (b). Due to higher absorption coefficient within the cooling tail E||c polarization was selected for the test.

Figure A26 shows redshift in $\lambda_f(T)$, $\alpha_r(\lambda,T)$ and MAT curve for 1% Ho:YLF sample. In Fig. A26 (a), the redshifts in $\lambda_f(T)$ for cooling grade 1% Tm:YLF and 1% Ho:YLF crystals are compared, which corresponds to the narrower ground state and excited state manifolds in Ho:YLF crystal. It is notable that the redshifts in $\lambda_f(T)$ for 1% Ho:YLF sample is very close to the optimal 5% Yb:YLF sample. Such a small shift in $\lambda_f(T)$ makes this crystal a promising candidate for optical cryocooler applications. In Fig. A26 (b), $\alpha_r(\lambda,T)$ of the sample is shown and in Fig. A26 (c), the global MAT of 130 K at 2070 nm is estimated for the sample. This is the first cooling demonstration of any Ho-doped material.

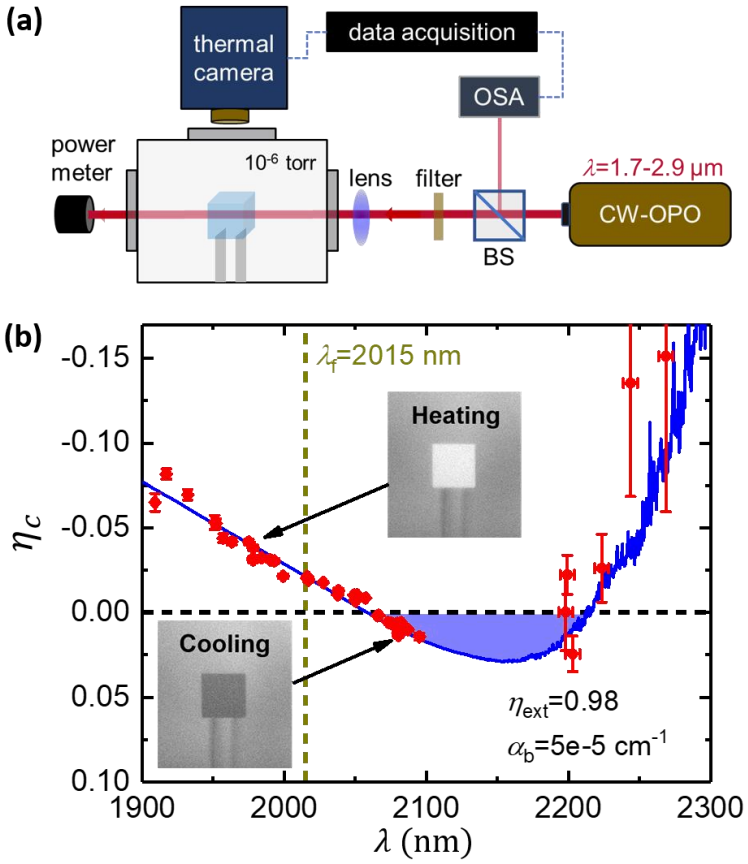

***Figure A25**: (a) Schematic of LITMoS test setup for 1% Ho:YLF sample, (b)cooling efficiency of 1% Ho:YLF crystal in E||c polarizations.*

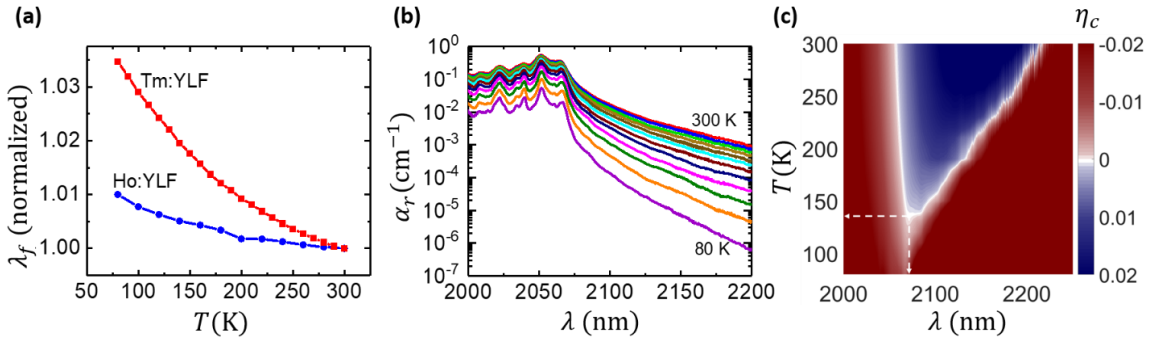

Figure A26: *(a) Temperature dependent mean emission wavelength $\lambda_f(T)$, (b) Temperature dependent resonant absorption coefficient $\alpha_r(\lambda, T)$ and (c) MAT curve for 1% Ho:YLF in E∥c polarization.*

There are several advantages in optical refrigeration of Ho-doped crystals. First, the width of energy manifolds is comparable with Yb ions, so the mean emission wavelength shift is very close to the best ever cooled crystal. Second, due to the abrupt changes in $\alpha_r(\lambda, T)$ within the cooling tail, improving the EQE of Ho-doped crystals would greatly enhance laser cooling results since it increases α_r within the cooling regime considerably. For instance, just 0.5% improvement in EQE (η_{ext}=0.985) would rsult in global MAT of 90 K with the same parameters that are shown in Fig. A25 (b). Further improvement in EQE and doping concentration of Ho ions, would result in sub-80 K MATs which are very beneficial for mid-IR optical cryoccoler applications. Considering our experimental result for Tm:BYF crystal with extremely high EQE (η_{ext}~0.999), it would be feasible expectation that Ho:BYF crystals with very high EQE be the best candidate for optical cryoccolers. On the other hand, such improvements would provide us with longer cooling window which is very important for development of mid-IR RBLs in Ho:YLF crystals. Figure A27 shows estimations of the global MATs to be 90 K and sub-80 K for 1%Ho:YLF crystal via improvement of EQE from 0.980 to 0.985 and 0.995. The reason why Fig. A27 (b) doesn't show sub-80 K temperatures is that our measurments for $\alpha_r(\lambda, T)$ was limited to 80 K since we used a Liquid Nitrogen cooled cryostat in that measurment.

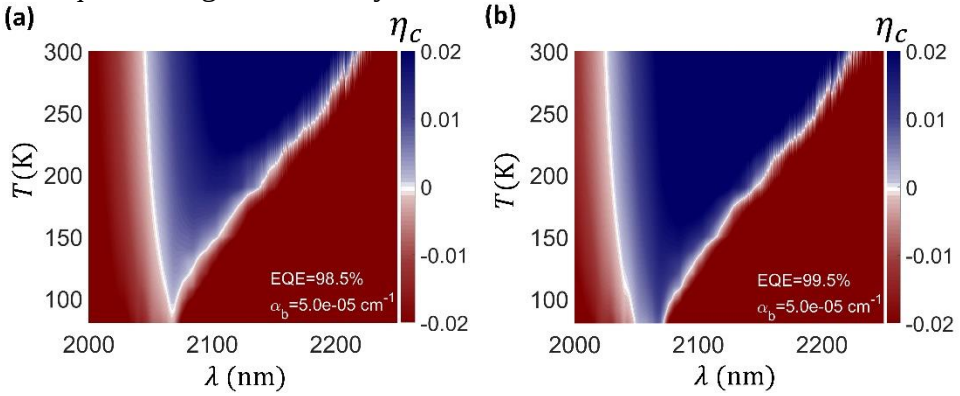

Figure A27: *Estimated Minimum Achievable Temperatures (MATs) of 1% Ho:YLF with α_b=5e-5 cm^{-1} and (a) η_{ext}=0.985 or (b) η_{ext}=0.995 in E∥c polarization.*

5 Journal Publications:

Total Citations (Google Scholar, 9/25/18): 52

1. Markus P. Helen, Junwei Meng, Alexander R. Albrecht, Eric R. Lee, Aram Gragossian, Steven P. Love, Christopher E. Hamilton, Richard I. Epstein, Mansoor Sheik-Bahae, “First demonstration of an all-solid-state optical cryocooler”, Light: Science & Applications 7: 15 (2018)

2. Saeid Rostami, Alexander R. Albrecht, Azzurra Volpi, Mansoor Sheik-Bahae, “Observation of optical refrigeration in a holmium-doped crystal” Light: Science & Applications, *under review* (2018)

3. A Gragossian, J Meng, M Ghasemkhani, AR Albrecht, M Sheik-Bahae, "Astigmatic Herriott cell for optical refrigeration", Optical Engineering 56 (1), 011110-01111 (2016)

4. C Wang, M Sheik-Bahae, "Determination of external quantum efficiency in semiconductors using pulsed power-dependent photoluminescence," Optical Engineering 56 (1), 011106-011106 (2016)

5. Seth D. Melgaard, , Alexander R. Albrecht, , Markus P. Hehlen, & Mansoor Sheik-Bahae, "Solid-state optical refrigeration to sub-100 Kelvin regime," Scientific Reports 6, Article number: 20380 (2016)

Conference Presentations (2015-2018):

5 invited talks (SPIE Photonics West, SPIE DCS, CLEO), one invited tutorial (DPC, Paris), 6 contributed

Patent Application:

A. Albrecht, J. Meng, M. Sheik-Bahae, “CTE-matched Textured Heatlinks with High Light Rejection Factors for Optical Refrigeration” (provisional, UNM, 2018)